

CHARGE CARRIER DYNAMICS OF METHYLAMMONIUM LEAD-IODIDE PEROVSKITE SOLAR CELLS

FROM MICROSECONDS TO MINUTES

Master-Thesis
Martin Neukom

Albert-Ludwigs-University Freiburg
Master Online of Photovoltaics
January 2016

Martin Neukom: *Charge Carrier Dynamics of Methylammonium Lead-Iodide Perovskite Solar Cells, From Microseconds to Minutes*, 2016

ABSTRACT

1.1 ENGLISH ABSTRACT

Transient opto-electrical measurements of methylammonium lead iodide (MALI) perovskite solar cells (PSCs) are performed and analyzed in order to elucidate the operating mechanisms. The current response to a light pulse or voltage pulse shows an extraordinarily broad dynamic range covering 9 orders of magnitude in time – from microseconds to minutes – until steady-state is reached. Evidence of a slowly changing charge density at the perovskite layer boundaries is found, which is most probably caused by mobile ions. Current-voltage curves (IV curves) are measured with very fast scan-rate after keeping the cell for several seconds at a constant voltage as proposed by Tress et al. Numerical drift-diffusion simulations reproduce the measured IV curves using different distributions of ions in the model. Analysing the band diagram of the simulation result sheds light on the operating mechanism. To further investigate the effects at short time scales (below milliseconds) photo-generated charge extraction by linearly increasing voltage (photo-CELIV) experiments are performed. We postulate that mobility imbalance in combination with deep hole trapping leads to dynamic doping causing effects from microseconds to milliseconds. Comprehensive transient drift-diffusion simulations of the photo-CELIV experiments strengthen this hypothesis. This advanced characterization approach combining dynamic response measurements and numerical simulations represents a key step on the way to a comprehensive understanding of device working mechanisms in emerging perovskite solar cells.

1.2 GERMAN ABSTRACT

In der vorliegenden Arbeit werden Methyl-Ammonium Perovskite-Solarzellen analysiert mit transienten optisch-elektrischen Messungen, um die physikalischen Prozesse zu untersuchen. Der transiente Photostrom, erzeugt durch einen Lichtpuls, zeigt eine ausserordentliche lange Dynamik über 9 Grössenordnungen in der Zeit - von Mikrosekunden bis Minuten - bis ein stationärer Zustand erreicht ist.

Es werden Belege präsentiert für langsam ändernde Ladungsträger-Dichten am Rand der Perovskit-Schicht, die sehr wahrscheinlich durch mobile Ionen innerhalb der aktiven Schicht verursacht werden. Es werden Strom-Spannungs-Kennlinien gemessen mit schnellen Spannungsrampen, nachdem die Zelle eine Weile auf bestimmter Spannung gehalten wurde, wie von Tress et al. vorgeschlagen. Die gemessenen IV-Kurven werden durch numerische Drift-Diffusions-Rechnungen mit verschiedenen Ionenverteilungen reproduziert. Die Analyse der Banddiagramme der Simulationsresultate zeigen dabei die Funktionsweise der Solarzelle auf.

Um die Solarzelle im kurzen Zeitbereich (unterhalb von Millisekunden) zu untersuchen, werden [photo-CELIV](#) Experimente gemessen. Dabei wird die Theorie aufgestellt, dass unausgewogene Ladungsträgermobilitäten in Kombination mit Loch-Traps zu dynamischer Dotierung des aktiven Materials führt, die Effekte im Zeitbereich zwischen Mikrosekunden und Millisekunden verursacht. Diese Hypothese wird gestärkt durch umfassende transiente Drift-Diffusions Simulationen der [photo-CELIV](#)-Ströme.

Diese umfassende Methode zur Charakterisierung, die dynamische Messungen mit numerischer Simulation verknüpft, zeigt den Weg auf zu einem umfassenden Verständnis der physikalischen Prozesse innerhalb von Perovskite-Solarzellen.

CONTENTS

1	ABSTRACT	3
1.1	English Abstract	3
1.2	German Abstract	4
I	INTRODUCTION	7
2	ECONOMICAL AND POLITICAL INTRODUCTION	9
2.1	Climate Change	9
2.2	Energy Markets and Photovoltaics	11
2.3	Cost Development	13
3	TECHNICAL INTRODUCTION	15
3.1	Photovoltaic Technologies	15
3.2	The Rise of Perovskite Solar Cells	18
II	METHODS	23
4	DEVICE FABRICATION	25
5	EXPERIMENTAL SETUP	27
6	SIMULATION MODEL	31
6.1	Model Equations	31
6.2	Model Parameters and Quantities	33
6.3	Perovskite Simulation Model	35
7	RC CORRECTION	37
7.1	Determining series resistance and capacitance	37
7.2	Derivation of the RC-Current Correction	38
III	SOLAR CELL PHYSICS	41
8	SOLAR CELL PHYSICS	43
8.1	General Principle	43
8.2	Driving Forces and Band Diagrams	44
8.3	Band Diagrams and Basic Solar Cell Operation	45
8.4	Majority versus Minority Carrier Devices	46
8.5	Recombination and Open-Circuit Voltage	50
IV	RESULTS AND DISCUSSION	57
9	RESULTS	59
9.1	IV Curve Hysteresis	59
9.2	Transient current response from microseconds to minutes	59
9.3	Slow Regime (Milliseconds to Minutes)	62
9.4	Fast Regime (Microseconds to Milliseconds)	67
9.5	Limitation of the approach	74
10	DISCUSSION	75
10.1	Time Dependent Charge Generation	75
10.2	Dipoles, Interface-Traps and Ferroelectricity	75

10.3	Excluding specific fabrication issues	76
10.4	Open Questions	76
V	SUMMARY AND OUTLOOK	77
11	SUMMARY	79
12	OUTLOOK	81
13	ACKNOWLEDGEMENT	83
VI	APPENDIX	85
14	APPENDIX	87
14.1	Abbreviations	87
15	BIBLIOGRAPHY	89

Part I

INTRODUCTION

ECONOMICAL AND POLITICAL INTRODUCTION

2.1 CLIMATE CHANGE

Stabilizing the global climate is one of the largest challenges of humanity in this century. The most recent report of the intergovernmental panel climate change IPCC [1] shows that human influence on climate change is evident.

From a scientific perspective climate change caused by greenhouse gas emission is evident.

"Human influence on the climate system is clear. This is evident from the increasing greenhouse gas concentrations in the atmosphere, positive radiative forcing, observed warming, and understanding of the climate system.", Working Group 1, Assessment Report 5, IPCC, 2013.

Figure 1 shows the annual average temperature rise on the globe within the last century. Global temperature rose by 0.8 degree in average within this period.

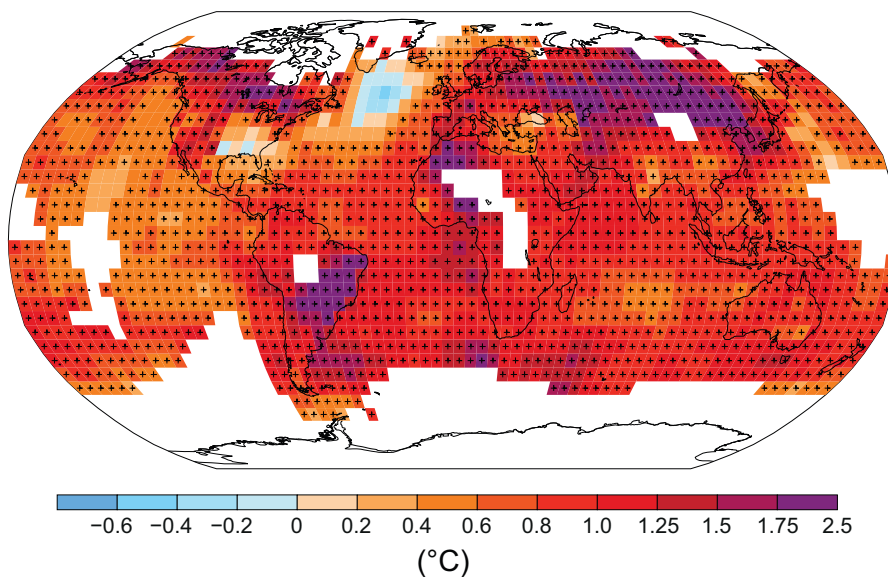


Figure 1: Map of the observed surface temperature change from 1901 to 2012.

Reprint from IPCC report WG1, AR5 [1].

The combustion of fossil energy sources like oil, gas and coal forms carbon dioxide CO_2 that has accumulated in the atmosphere and in the ocean over the last century. This has led to an increase in CO_2 concentration in the atmosphere from 280 ppm (0.028%) up to 400 ppm (0.040%). Greenhouse gases can be regarded as thermal isolation for the planet enabling a temperature range suited for life on

Burning fossil fuels has led to a strong increase in CO_2 concentration in the atmosphere.

CO₂ remains in the atmosphere for centuries. Climate change therefore persists over dozens of generations.

this planet. The physical origin is the absorption and re-emission of thermal radiation. Changing the concentration of greenhouse gases in the atmosphere leads to a change in isolation and therefore to a temperature increase.

As CO₂ is a highly non-reactive gas, it remains in the atmosphere for several hundred years. The human influence on the climate therefore persists over centuries and affects dozens of future generations.

"Warming of the climate system is unequivocal, and since the 1950s, many of the observed changes are unprecedented over decades to millennia. The atmosphere and ocean have warmed, the amounts of snow and ice have diminished, sea level has risen, and the concentrations of greenhouse gases have increased.", Working Group 1, Assessment Report 5, *IPCC*, 2013.

The Intergovernmental Panel Climate Change (*IPCC*) has estimated the expected global temperature rise for different emission scenarios. The modelled mean temperature rise is shown in [Figure 2](#) for two representative concentration pathways (*RCPs*). Please note that this temperature increase is in addition to the presently observed mean increase as shown in [Figure 1](#).

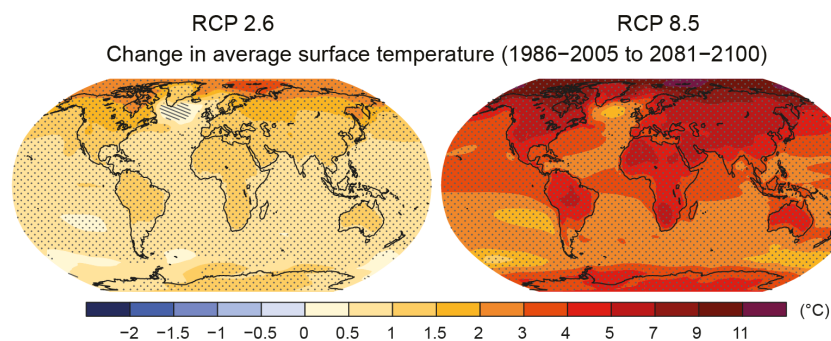


Figure 2: Model result for average surface temperature change for scenario [RCP 2.6](#) and [RCP 8.5](#).

Reprint from IPCC report WG1, AR5 [1].

[RCP 2.6](#) corresponds to cumulative emissions between 2012 and 2100 of 1000 Gt CO₂, the scenario [RCP 8.5](#) to 6000 Gt CO₂, respectively.

An average temperature rise has major implications of life on earth, like water scarcity, more intense weather extremes and monsoons, global sea level rise, droughts and major implications on food production.

The CO₂ concentration in the ocean and the average temperature rise has major implications on life on earth. Since warmer air can take up more moisture, precipitation increases in some regions, whereas in others it decreases leading to droughts. Water as a resource will generally become more scarce and is expected to be a source of conflicts in the future. Water scarcity will furthermore lead to a reduction in agriculture.

Weather extremes occur more frequently and increase in intensity. Monsoons are expected to become more intense. The melt-down of

glaciers, greenland and antarktis lead to a global sea level rise threatening whole island nations and civilizations on shallow land close to oceans. Furthermore the take-up of CO₂ leads to an acidification of the oceanic water threatening corals and other species.

Most discussions about consequences of climate change are based on a 2 degree scenario, what corresponds to RCP 2.6. Climate change is already in full progress and many of the mentioned consequences become more and more a reality. The issue of climate change is not longer a question of avoiding - it is a question of damage reduction. Scenarios like RCP 8.5 would have enormous consequences and additional climate feed-backs would be triggered such as the release of methane from Siberian permafrost that is melting. The Arctic ice is completely molten by the end of this century in scenario RCP 8.5.

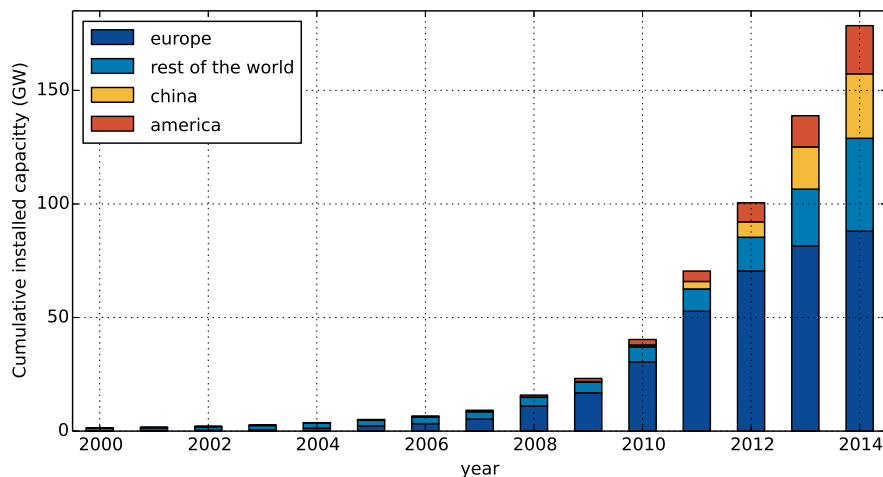
To avoid the danger of climate change on cost of future generations it is of crucial importance to stop emitting greenhouse gases. In the authors view it is the largest challenge of this centuries' societies, requiring change in social structure, change of political legislations as well as development and implementation of green technologies.

The issue of climate change is not longer a question of avoiding - it is a question of damage reduction.

Changing the societies from fossil-based to renewable is a major requirement to effectively protect the climate.

2.2 ENERGY MARKETS AND PHOTOVOLTAICS

The photovoltaic industry has grown tremendously in the past ten years. At the end of 2014 the total installed photovoltaic power reached 178 GW_p as shown in Figure 3. The industry association SolarPower Europe estimates that the cumulative installed power could reach half a terawatt in 2020 [2].



At the end of 2014 the total installed PV power reached 178 GW_p

Figure 3: Cumulative installed photovoltaic peak power worldwide.

Data source: SolarPowerEurope [2].

Due to a strong reduction in support schemes for renewable energy the growth in Europe has slowed down. But Europe remains

the region with the largest PV installation. In 2014 China was the biggest market - more than 10 GW have been newly installed in 2014.

The amount of installed peak power of photovoltaics cannot be directly compared to other sources of energy since the **full load hours** vary significantly. Therefore the total amount of generated electricity per year is plotted in **Figure 4** to compare electricity generation from wind, PV, nuclear, hydro and fossil thermal electricity production. Please note that fossil fuels for heating or transportation is not considered in this graph.

Different energy sources for electricity generation are compared by its global annual energy production.

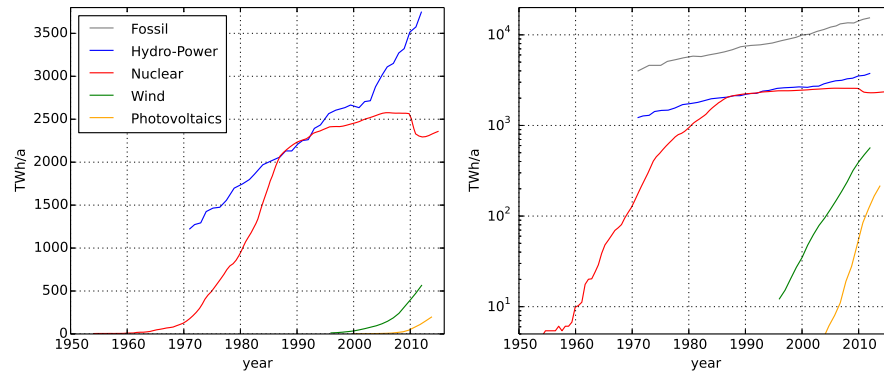


Figure 4: Annual worldwide produced electricity by technology. Both graphs show the same information, on the left in linear y-scale, on the right in logarithmic y-scale.

*Data Source: PV power from SolarPower Europe[2] with assumed **full load hours** of 1100 h. Wind power from Global Wind Statistics [3] with assumed **full load hours** of 2000 h. Nuclear, hydro and fossil production from IEA Key World Energy Statistics [4].*

The nuclear industry experienced a boom starting in the 1970 increasing to an energy production of about 2500 TW/a. After the first nuclear catastrophe in Tschernobyl in 1986 its growth decreased whereas after the explosion of the nuclear power plant in Fukushima in 2011 the worldwide nuclear energy production even dropped.

Nowadays wind and PV grow as fast as the nuclear electricity production during its boom phase in the 1980s.

Today (2015) in Greece, Italy and Germany solar power produces more than 7% of the total electricity demand [2]. On a global level the PV production is still on a low level compared to the annual hydro, nuclear and fossil electricity production. The total PV production reached about 10% of nuclear and 1% of fossil fuel production. A look at the growth rates in **Figure 4** shows that PV and wind are growing as fast as the nuclear energy did in the 1980. The trend is clear: In Europe in 2014 19.9 GW power of renewable energy sources was installed whereas nuclear power did not change and coal, oil and gas electricity production capacities have been decommissioned[2].

2.3 COST DEVELOPMENT

The price of photovoltaic modules experienced an unforeseen decline while power conversion efficiencies went up. Figure 5a shows the price development from 25 Euros per Watt-Peak in 1980 down to below 50 Eurocent in 2014 [5].

The price experience factor for silicon PV modules was about 20 % in the last 35 years, meaning that for every doubling of the worldwide cumulated produced capacity the price was reduced about 20 %. This effect is shown in the price experience curve in Figure 5b.

The cost of PV modules decreased tremendously in the past 40 years. With every doubling of cumulated installed power prices decreased by 20%.

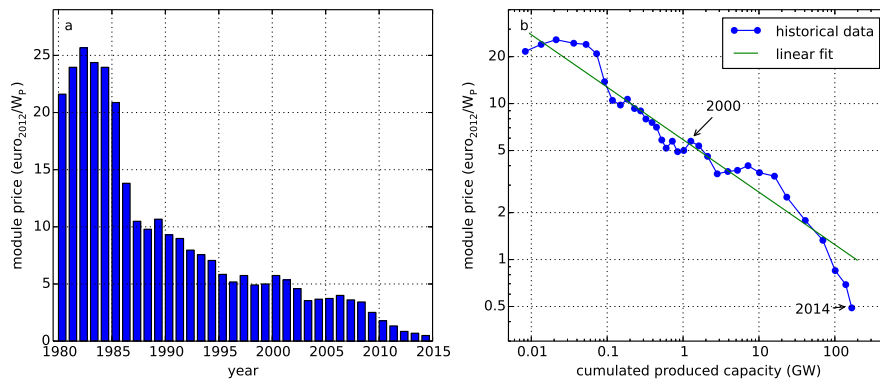


Figure 5: a) Development of average module prices. b) Price experience curve of PV modules with a price experience factor of 20 %.

Data source: Agora Energiewende [5] and ISE PV report [6].

With the prices of modules also the levelized cost of electricity dropped. When the *Erneuerbare-Energien-Gesetz* (EEG) was introduced in 2004 in Germany the feed-in tariff for rooftop photovoltaics was close to 60 eurocent/kWh whereas in 2014 it was below 14 eurocent/kWh [7]. Figure 6 shows the development of the feed-in tariffs for PV in Germany and Switzerland. This enormous decline of production cost was unforeseen or ignored by many conventional actors in the electricity production. The Swiss electricity supplier Axpo for example estimated in a report 2010 the cost of PV for the year 2030 to be between 30 and 42 Rp./kWh[8]. Already five years after the report the Swiss feed-in tariff was well below as shown in Figure 6. This underestimation, which is by far not an exception, shows the huge dynamics of the PV industry in the past 10 years.

Many actors in the electricity production heavily underestimated the dynamics of cost development in the PV sector. Today PV electricity is less expensive than electricity from the grid (grid parity).

Meanwhile the cost of a PV module is less than half of the system costs. Planing, installation, cables and the inverter make up the other half. As the cost reduction potential of the installation is limited, the module efficiency gets more and more important for the total system costs. System costs are usually given in Franks per watt peak (CHF/kW_p) - Increasing the module power therefore decreases the total costs of the system.

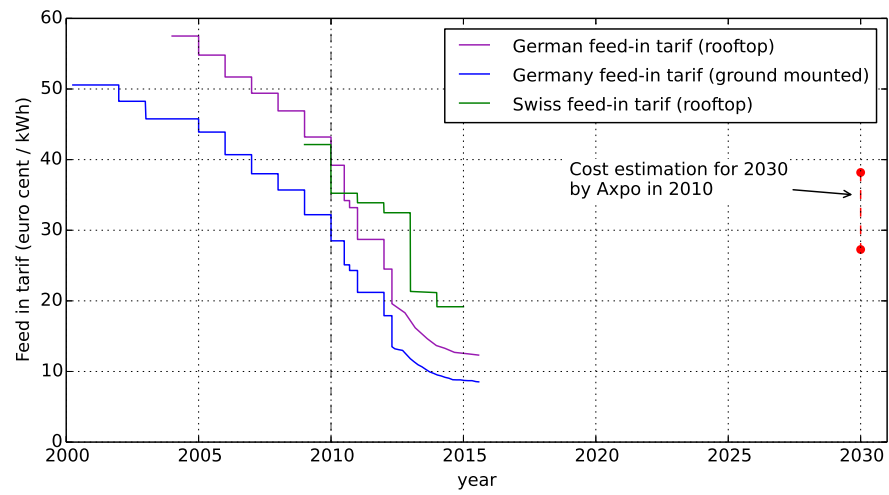


Figure 6: Development of feed-in tariffs for photovoltaics in Germany and Switzerland[7, 9]. In red on the right the cost estimation for 2030 by Axpo, a major electricity supplier in Switzerland, is shown[8].

TECHNICAL INTRODUCTION

3.1 PHOTOVOLTAIC TECHNOLOGIES

In this section the main commercially relevant solar cell technologies are discussed and compared with the novel technologies organic solar cells (OSC), dye sensitized solar cells (DSSCs) and methylammonium lead iodide (MALI) perovskite solar cells (PSCs). To keep this section short other technologies and materials like organic hybrids, gallium-arsenide (GaAs), quantum dot or all types of concentrator cells are not treated.

3.1.1 Crystalline Silicon Solar Cells

Crystalline silicon is the most widely used material to produce solar cells and covers more than 90 percent of the global market size. The highly purified silicon crystal is cut with a wire-saw in slices. These are then connected in series to create a module. The wafers are either made from a single crystal¹ (higher cost, higher efficiencies) or from a poly-crystalline² ingot (lower cost, lower efficiency).

Due to economy of scale effects this elaborate technique became extremely cheap, as shown in the previous section. The optical absorption of silicon solar cells is comparably weak, such that wafers need to be around 150 μm thick to absorb most of the light. Due to the high material quality the charge carrier diffusion length is large enough for the carriers to leave the device via diffusion.

Silicon PV is currently the dominant technology in the market. Modules are produced from single wafers of crystalline silicon. Compared to other technologies it is rather thick (150 μm).

3.1.2 CdTe and CIGS

The materials cadmium telluride (CdTe) and copper indium gallium diselenide (CIGS) are the two most prominent compound semiconductors used in photovoltaics. Both materials are strong absorbers such that they can be made thin - A CdTe layer is about 8 μm thick and CIGS layer is about 2 μm thick. Both technologies are deposited on glass via co-evaporation, metal organic chemical vapor deposition (MOCVD) or other deposition techniques. In both cases monolithic integration is used to create a module.

Since cadmium is highly toxic the large scale application of CdTe solar cells is controversial. The CdTe compound is however non-

CdTe and CIGS are deposited on a substrate to create thin-film solar cells. A module is built by monolithic integration.

¹ Also called mono-crystalline.

² Also called multi-crystalline.

toxic and strongly bound chemically, such that elevated temperatures above 1000 degree Celsius are required to dissolve the cadmium.

As indium and gallium are rare and expensive the use of combinations of more abundant materials is tested such as copper zinc tin sulfur (CZTS) reaching currently an record efficiency of 12.6% [10].

3.1.3 Amorphous Silicon

Amorphous silicon has a much stronger absorption than its crystalline form. It can therefore be used as thin film. Due to its low material quality efficiencies are much below classical wafer-based silicon.

In amorphous silicon solar cells silicon is deposited on a substrate to form a thin amorphous film. Amorphous silicon is a direct semiconductor and has therefore a much higher absorption than its crystalline form. Due to a large amount of defects in the material the electrical quality is much lower than in crystalline silicon resulting in clearly lower efficiency.

Amorphous silicon can be used in a [tandem](#) configuration with micro-crystalline silicon resulting in higher power conversion efficiencies (PCE). Since crystalline silicon has become very cheap in the recent years, amorphous silicon has lost of relevance for power production.

Other applications are possible since amorphous silicon can be deposited on flexible substrates.

3.1.4 Novel technologies

Novel technologies offer cheaper production, light-weight or flexibility.

A number of novel photovoltaic materials and concepts are investigated by researchers. The goal is to create solar cells that are either more efficient, less expensive or flexible, light-weight or transparent. Possible applications of such would be transparent solar cells³, solar cells on mobile devices or the use as design element (for example Solarte by Belectric [11]).

A [DSSC](#) uses different materials for charge absorption and transport. A dye absorbs the photons - The electrons are rapidly transferred to an electron conductor (usually mesoporous TiO_2) and holes are transported by a liquid electrolyte. [MALI](#) perovskite solar cells were first fabricated as [DSSC](#) [12]. Perovskite solar cells are introduced in the next chapter.

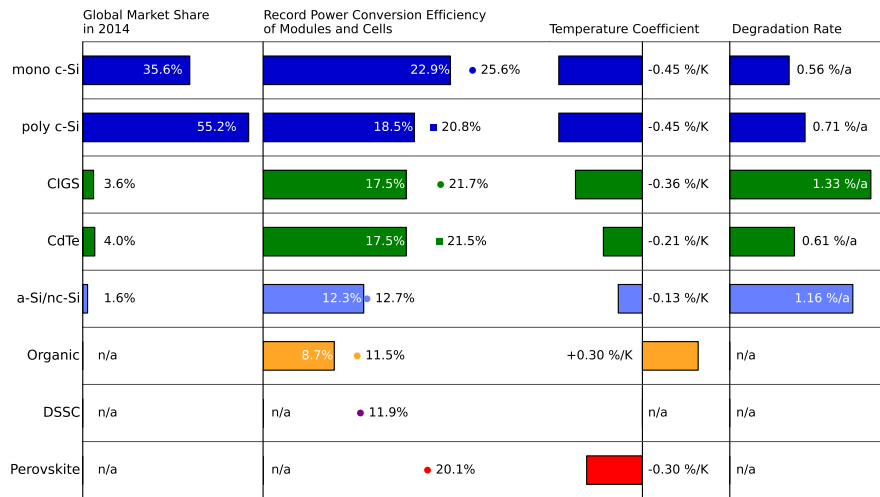
Organic solar cells are very strong absorbers and can therefore be made very thin (100 nm).

An organic solar cell ([OSC](#)) is made from organic molecules (a molecule that includes a carbon atom) that are either evaporated or solution-processed. The organic absorber materials have a very strong absorption such that it is sufficient to use an active layer thickness of 100 nm. One main obstacle of [OSC](#) is the high [exciton](#) binding energy

³ It may need to be mentioned, that transparent solar cells are by definition not very good absorbers. Efficient power conversion cannot be expected from this type of device.

caused by the low dielectric constant. The thermal energy at room temperature is not sufficient to dissociate an **exciton** into free charge carriers. An interface between two materials with different energy level is required. In state-of-the-art organic solar cells two materials are mixed in a so called bulk-heterojunction. Because some energy is lost at the dissociation of **excitons** the maximum achievable **PCE** is lower than for other techniques [13].

3.1.5 Technology Overview



The market share, record efficiency for modules and cells, the temperature coefficient and degradation rates of the mentioned technologies are compared.

Figure 7: Overview over the commercially relevant solar cell materials and the novel technologies. Dots indicate the record **PCEs** for cells, the bars the module records. For the novel technologies (**OSC**, **DSSC** and **perovskite**) there is no reliable degradation data yet and they are not yet commercially available.

Data source: Market share from ISE PV report [6]. Record PCE from solar cell efficiency tables version 46 [10] and NREL [14]. Temperature coefficients from Virtuani [15], **OSC** estimation from Katz and Riede [16, 17], **Perovskite** from Jung [18]. Degradation data from Jordan [19].

Figure 7 provides an overview over the various solar cell technologies. As mentioned above crystalline silicon dominates currently the market. With 22.0 % mono-crystalline modules have clearly the highest power conversion efficiency [10].

Most technologies have a negative temperature coefficient as shown in Figure 7, except **OSC**. The charge transport of these systems is temperature activated leading to higher currents at elevated temperatures. This is an advantage over other technologies.⁴

The degradation rate stems from a literature survey about published

Except for organic solar cells the power output of a module decreases with temperature.

⁴ However, the crystalline silicon module with 22.9 % **PCE** would need to reach a temperature of 163 degree Celsius to have the same efficiency as the **OSC** module at room temperature.

degradation data [19] and can vary significantly. With a degradation rate below 1% it takes more than 22 years for the module to reach 80% of its initial performance.

3.2 THE RISE OF PEROVSKITE SOLAR CELLS

NREL regularly publishes the evolution of record power conversion efficiencies of the major cell technologies.

Figure 8 shows the evolution of published record power conversion efficiencies (PCE) - a well known graph published regularly by the National Renewable Energy Laboratory (NREL). It seems that for silicon solar cells the maximum achievable power conversion has been reached. For CIGS and CdTe there has been remarkable improvements in the last five years.

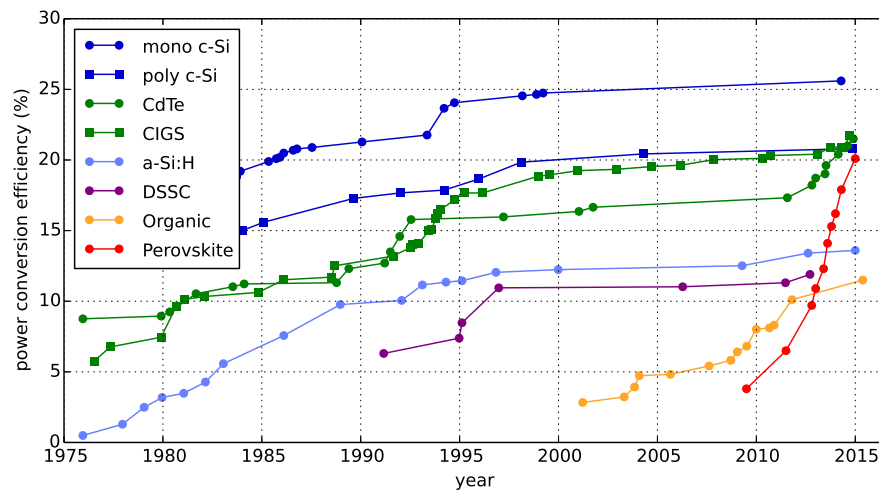


Figure 8: Published record power conversion efficiencies for different cell technologies.

Data Source: Perovskite evolution from Park [20] other data from NREL [14].

Perovskite solar cells have experienced an unprecedented rise in efficiency up to 20.1% and got a lot of attention in the research community.

Looking at Figure 8 is it evident why methylammonium lead iodide (MALI) perovskite solar cells (PSCs) got a lot attention in the research community lately. The record power conversion efficiency went up to 20.1% although this material was unknown in the PV community five years ago.

There are a couple of reasons why perovskite solar cells are highly efficient and of big interest for the community:

- High optical absorption with a sharp absorption onset
- High charge carrier mobility
- Long charge carrier lifetimes
- Balanced charge transport
- High open-circuit voltages can be reached (up to 1.2 V)

- The band-gap can be adjusted (mixed halide perovskites)
- Low-cost fabrication

The material itself has been known in science for decades, but no attention was paid to its photovoltaic properties. In 2009 the **MALI** perovskite was first used by Kojima in a **DSSC** structure [21]. This work was not particularly noticed since the efficiency was about 3% and the device was unstable due to the liquid electrolyte. Perovskite solar cells got broad attention after Nam-Gyu Park's group published a stable device with 9.7% efficiency [22].

The first perovskite solar cell was published in 2009.

3.2.1 Perovskite Material

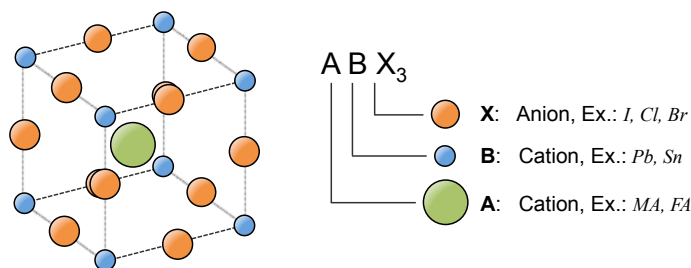


Figure 9: Unit-cell of a perovskite structure.

Perovskite was initially the name for a mineral well-known as calcium titanium oxide ($CaTiO_3$) [23]. Now the name perovskite is mainly used to describe a crystal structure. It has the general structure ABX_3 as shown in Figure 9 where:

- **A** is a cation. In most cases an organic molecule is used like methylammonium (MA) $CH_3NH_3^+$ or formamidinium (FA) $HC(NH_2)_2^+$.
- **B** is a cation that is normally either lead (Pb) or tin (Sn). To tune the material properties lead and tin can also be mixed.
- **X** is an anion where iodine (I), chloride (Cl) or Bromide (Br) is used. Often these atoms are mixed to tune the bandgap.

The standard material combination is methylammonium lead iodide (**MALI**) $CH_3NH_3PbI_3$ but various other material combinations have been studied [18] such as: $CH_3NH_3PbI_3$, $CH_3NH_3PbI_{3-x}Cl_x$, $CH_3NH_3PbBr_3$, $CH_3NH_3Pb(I_{1-x}Br_x)_3$, $HC(NH_2)_2PbI_3$, $HC(NH_2)_2Pb(I_{1-x}Br_x)_3$, $CH_3NH_3SnI_3$.

Recently a perovskite solar cell employing bismuth has been published [24] reaching an efficiency below 1%.

MALI perovskite can be produced with either by a solution process or by vacuum deposition [25]. The perovskite films deposited with

*Perovskite is a crystal structure, not a material. The most common material combination for solar cells with perovskite structure is methylammonium lead iodide (**MALI**).*

Perovskite *MAL* is poly-crystalline and deposited either by solution or with a vacuum process.

these techniques are poly-crystalline with crystal sizes from several hundreds of nanometers to micrometers. Nie et al. published *PSC* with grain sizes up to millimeters [26].

Calculations by density functional theory (*DFT*) have shown that grain boundaries in perovskite show remarkably low mid-bandgap states [27]. This is probably one of the origins of the charge carrier recombination in these materials.

3.2.2 Perovskite Device Structure

Perovskite can be applied in different solar cell architectures as illustrated in *Figure 10* using a variety of contact materials. In all three cases the layers are deposited on top of a glass with transparent conducting oxide (*TCO*). The perovskite layer is then sandwiched between an electron transport layer (*ETL*) and hole transport layer (*HTL*) with a back contact of gold or aluminium.

Perovskite solar cells are used either in a meso-porous scaffold with TiO_2 or Al_2O_3 or in a planar structure.

First published perovskite solar cells used porous TiO_2 structure where the perovskite was infiltrated into. In these structures electrons can be transported either in TiO_2 or in the perovskite whereas the holes are transported only in the perovskite. Lee et al. replaced the conducting TiO_2 with isolating Al_2O_3 resulting in a higher open-circuit voltage. [28]. In these structures charge transport occurs solely in the perovskite layer.

These finding made clear that perovskite could also be used in a planar device structure omitting the mesoporous layer. The group of Henry Snaith published in 2013 the first planar structure reaching efficiencies of 15% [29].

Following materials have been used as contact layers [18]:

ETL: TiO_2 , PCBM, ZnO

HTL: spiro-OMeTAD, P3HT, PEDOT:PSS, PCBTDP, PTAA

Depending on the deposition process of the materials standard or inverted structures have been used. In the standard structure the electrons move to the front side (*TCO*) and holes to the backside of the solar cell whereas in the inverted structure it is vice-versa as shown in *Figure 10*.

3.2.3 Extraordinary Physical Effects

Many aspects of the physical working mechanism of *PSCs* remains under debate.

Despite this fast and unprecedented rise of PCE many aspects of the device physics still remain under debate.

PSCs show extraordinary effects like current-voltage (*IV*) curve hysteresis [30], slow transient effects [31–34], very high capacitance at low frequency [35] and switchable photovoltaics [36, 37]. To explain the origin of these effects, different mechanisms have been proposed

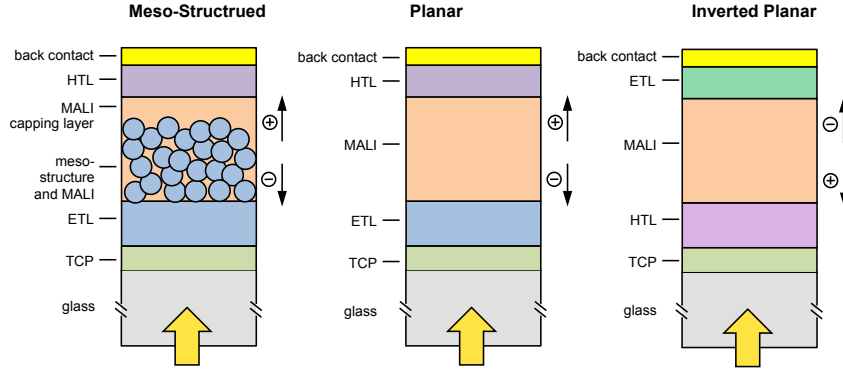


Figure 10: Different solar cell architectures employing perovskite.

including interface traps and contact resistance between the TiO_2 and MALI layers [30], defects and traps at the $FTO - TiO_2$ layer interface [38], ferroelectricity and ordering of dipole orientations

[39–44], structural changes [32], bulk photovoltaic effect [45] and ion migration. There is indeed increasing evidence that ion migration is taking place and has implications on cell physics and achievable performance [31, 33, 37, 46–48].

Perovskite solar cells show further remarkable effects. Depending on growth conditions MALI can be n-type or p-type as shown by first principle calculations [49]. Reversible photo-induced trap formation has been shown for mixed halide perovskites [50]. Like all ferroelectric materials MALI is piezoelectric and pyroelectric. MALI shows exceptionally low recombination [51] and very high PL efficiency. Furthermore optically pumped lasing has been demonstrated in $CH_3NH_3PbI_{3-x}Cl_x$ perovskites [52].

To explain the IV curve hysteresis different physical effects like ferro-electricity and mobile ions have been proposed in the literature.

Part II

METHODS

DEVICE FABRICATION

The perovskite solar cells characterized in this study were produced at the Institute of Microengineering (IMT) in Neuchatel according to the following procedure.

A solution-processed TiO_2 hole blocking layer was deposited on cleaned ITO substrates by spin coating twice a solution of 0.11 ml diisopropoxy-titanium bis(acetylacetonate) in 1 ml butanol and subsequent annealing at 500 degree C in air. On top of the blocking layer, a 270 nm thick TiO_2 mesoporous scaffold was deposited by spin coating a TiO_2 nanoparticle paste and sintering at 500 degree C in air. The sample was transferred to a nitrogen-filled glovebox, and the perovskite absorber layer was spin coated from a solution of 1.2 M PbI_2 and CH_3NH_3I dissolved in a 7:3 v/v mixture of γ - butyrolactone and dimethyl sulfoxide at 1000 rpm for 15 s and 5000 rpm for 30 s. At 10 seconds before the end of the second spin coating step, chlorobenzene was dripped onto the rotating substrate.

After annealing at 100 degree C for 10 min, 2,2',7,7'-Tetrakis-(N,N-di-4-methoxyphenylamino)-9,9'-spirobifluorene (spiro-OMeTAD) doped with Lithium was spin coated at 4000 rpm for 30 s. Finally, a 70 nm thick Au rear electrode was deposited by thermal evaporation through a shadow mask, defining a cell area of 0.25 cm².

The devices studied in this thesis are produced by solution employing a meso-porous TiO_2 layer as scaffold and electron contact and spiro-OMeTAD as hole contact.

EXPERIMENTAL SETUP

All experiments are performed using the all-in-one measurement system *Paivos 3.0* [53]. *Paivos* performs steady-state, transient and impedance measurements automated after each other. A function generator controls the light source - a white LED. A second function generator controls the applied voltage. The current and the voltage of the solar cell are measured with a digitizer. The current is measured via the voltage drop over a $20\ \Omega$ resistor or a transimpedance amplifier¹, depending on the current amplitude.

All experiments presented in this thesis are performed with the measurement system Paivos.

5.0.4 Flexible Time-Resolution (Flex-Res)

In this thesis transient current measurements are performed with very high dynamic range. Within the scope of this thesis the measurement system *Paivos* was extended for this purpose.

Traditional oscilloscopes use fixed time steps. If such a measurement is plotted with logarithmic time 90 % of the measurement points are in the last time decade. This leads to a low dynamic range as shown in Figure 11 (black line). The total number of measurement points is 3000. Between 100 ms and 1 s there are 2700 points whereas between 1 ms and 10 ms only 27 points are measured.

To measure TPC experiments over 7 orders of magnitude in time a special technique was developed named Flex-Res.

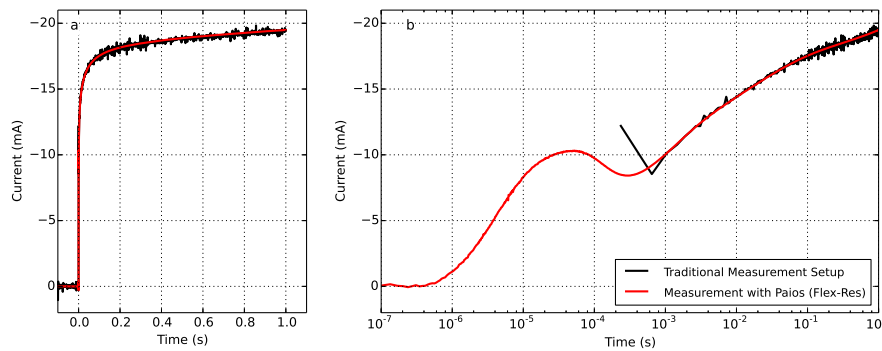


Figure 11: a) transient photocurrent (TPC) response of a perovskite solar cell with linear time scale. b) The same data but with logarithmic time scale. With linear time sampling 3 orders of magnitude can be resolved, whereas 7 orders of magnitude are possible with logarithmic time sampling (*Flex-Res*).

Therefore a procedure was developed where up to 30 million points are measured and a time-logarithmic re-sampling is performed. The

¹ With the transimpedance amplifier currents down to $1\ \text{nA}$ can be resolved.

time-logarithmic re-sampling is necessary because 30 million points take up too much memory and can hardly be processed.²

With this technique, named *Flex-Res*, transient currents can be resolved over 7 orders of magnitude. Figure 11 compares the traditional measurement with a measurement with *Flex-Res*. Apart from the higher time-resolution the second advantage is the increased current resolution at higher times. In the last decade of the *Flex-Res* measurement in Figure 11b, the current resolution is increased from 12 Bit to 20 Bit due to the averaging of 62'000 points.

5.0.5 Integration with Numerical Simulation

Numerical simulations are very useful to gain physical understanding. When simulating several experiments of several devices, data handling and optimisation can get very complex.

Numerical simulation of the absorption and charge transport is a very powerful tool to gain insight into physical processes. It is however also complex as many parameters play a role that are not precisely known. In this thesis more than 20 different experiments were performed on 10 different devices. Some experiments contain 20 measurement curves as experimental parameters are varied.

With this amount of data manual data handling, comparison with simulation and plotting is not only tedious - it is close to impossible.

This problem is solved by tight and seamless integration of measurement, processing, data storage and simulation. These improvements are made available in the measurement system *Paivos* [53] of the company *Fluxim AG*.

The simulation software (*Setfos*) was seamlessly integrated into the measurement software (*Paivos*) to keep the overview over devices, experiments and parameters. Measurement and simulation can hereby directly be compared.

Figure 12 shows a screenshot of the *Paivos* measurement software with the integrated simulation software *Setfos* [54]. Hereby the *Paivos* measurement software is the master, that stores and manages all measurement data, simulation parameter and simulation results.

The *Paivos* software written in *LabView* and the *Setfos* software written in *Java* communicate over the local network. First *Paivos* searches the local network for available *Setfos*-Servers. As schematically shown in Figure 13 several *Setfos* servers can run on the same computer. To perform simulations *Paivos* can distribute simulation tasks among all *Setfos* instances enabling parallel computing.

The development of the *Setfos* - *Paivos* integration (SPI) was a major step that facilitated the analysis of perovskite solar cells presented in this thesis.

² If current, voltage and light intensity are measured with 30 million points in double-precision (64 Bit) 720 MB of memory is used. Efficient memory handling during the re-sampling is therefore crucial.

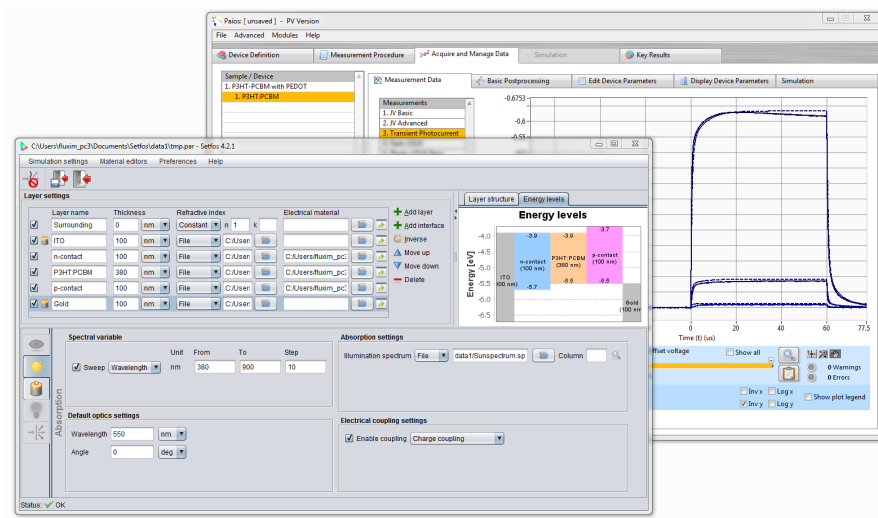


Figure 12: Seamless integration of the simulation software *Setfos* [54] and the measurement software *Paios* [53]. Measurement and simulation can directly be compared in the measurement software (simulation: dashed line, measurement: solid line).

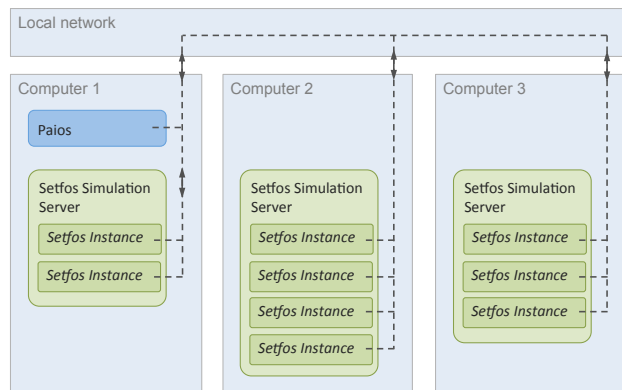


Figure 13: Schematic illustration of the communication of *Paios* with *Setfos* over the local network. *Paios* can manage several *Setfos*-Servers on different computers that allows parallel distributed computing.

SIMULATION MODEL

The physical model used in this thesis is implemented in the numerical simulation software *Setfos* 4.2 [54]. The absorption profile is calculated with a thin film optics algorithm [55, 56] considering the full solar cell stack from glass substrate to rear gold electrode. Complex refractive indices of perovskite are taken from Ref [57].

The charge continuity-equation in the drift-diffusion model is solved for electrons and holes coupled by the Poisson-equation. Charge doping is simulated by adding fixed space charge in the Poisson-equation. Direct electron-hole recombination is considered in the model. For simplicity Shockley-Read-Hall (SRH) recombination is neglected. The model is solved in a one-dimensional domain.

6.1 MODEL EQUATIONS

In this section the governing equations of the drift-diffusion model implemented in *Setfos* [54] are listed and explained. The quantities are listed at the end of the section.

The **continuity equation** for electrons and holes governs the change in charge carrier density due to current flow, recombination and generation.

$$\frac{\partial n_e}{\partial t}(x, t) = \frac{1}{q} \cdot \frac{\partial j_e}{\partial x}(x, t) - R(x, t) + G_{opt} \cdot g(x) \quad (1)$$

$$\frac{\partial n_h}{\partial t}(x, t) = -\frac{1}{q} \cdot \frac{\partial j_h}{\partial x}(x, t) - R(x, t) + G_{opt} \cdot g(x) \quad (2)$$

For the calculation of the charge generation $g(x)$ *Setfos* considers the measured illumination spectrum and refractive indices of each layer of the cell stack.

As **boundary conditions** the electron density at the anode and the hole density at the cathode are set to fixed values n_{e0} and n_{h0} .

$$n_e(0, t) = n_{e0} \quad (3)$$

$$n_h(d, t) = n_{h0} \quad (4)$$

First the absorption of photons is calculated. Then the drift and diffusion of charge carriers is computed. The models presented in this chapter are implemented in the software Setfos .

The continuity equation describes how electron and hole concentration changes over time.

Bimolecular recombination is used to annihilate electrons and holes.

The radiative **recombination** is proportional to the charge carrier density of electrons and holes.

$$R(x, t) = B \cdot n_e(x, t) \cdot n_h(x, t) \quad (5)$$

The charge current consists of a drift- and a diffusion-part.

The **currents of electron and holes** consist of drift in the electric field and diffusion due to the charge carrier density gradient.

$$j_e(x, t) = n_e(x, t) \cdot q \cdot \mu_e \cdot E(x, t) + \mu_e \cdot k \cdot T \cdot \frac{\partial n_e}{\partial x}(x, t) \quad (6)$$

$$j_h(x, t) = -n_h(x, t) \cdot q \cdot \mu_h \cdot E(x, t) + \mu_h \cdot k \cdot T \cdot \frac{\partial n_h}{\partial x}(x, t) \quad (7)$$

The total current includes particle- and displacement-current.

The **total current** is the sum of electron, hole current and the displacement current. This total current is constant in x .

$$j(x, t) = j_e(x, t) + j_h(x, t) + \frac{\partial E}{\partial t}(x, t) \cdot \epsilon_r \cdot \epsilon_0 \quad (8)$$

The Poisson equation is the first Maxwell equation, relating electric field and charge.

The **Poisson equation** relates the electric field with the charges inside the layer. Charge doping is added in form of fixed charge densities N_A and N_D .

$$\frac{\partial E}{\partial x}(x, t) = -\frac{q}{\epsilon_0 \cdot \epsilon_r} \cdot (n_h(x, t) - n_e(x, t) + N_A - N_D) \quad (9)$$

The electric field is the gradient of the potential.

The **cell voltage** is defined as the source voltage minus the built-in voltage and the voltage drop over the series resistance.

$$V_{Cell} = \int_0^d E(x, t) \cdot dx = V_{Source}(t) - j(t) \cdot S \cdot R_s - V_{bi} \quad (10)$$

The built-in field is the difference in [workfunctions](#).

The **built-in voltage** is defined as the difference in [workfunctions](#) of the electrodes. The workfunctions are calculated according to the boundary charge carrier density n_{h0} and n_{e0} .

$$V_{bi} = \frac{\Phi_A - \Phi_C}{q} \quad (11)$$

$$\Phi_A = E_{LUMO} - \ln\left(\frac{n_{e0}}{N_0}\right) \cdot k \cdot T \quad (12)$$

$$\Phi_C = E_{HOMO} + \ln\left(\frac{n_{h0}}{N_0}\right) \cdot k \cdot T \quad (13)$$

The equations above are solved on a one-dimensional grid either in steady-state, time-domain or in frequency-domain. The following quantities can be evaluated as post-processing.

The **potential** is evaluated according to:

$$\varphi(x_1, t) = \int_0^{x_1} E(x, t) \cdot dx \quad (14)$$

The **effective bands** are:

$$E_{CB}(x, t) = E_{LUMO} - q \cdot \phi(x, t) \quad (15)$$

$$E_{VB}(x, t) = E_{HOMO} - q \cdot \phi(x, t) \quad (16)$$

The **quasi Fermi levels** of electrons and holes are:

$$E_{fe}(x, t) = E_{CB}(x, t) + k \cdot T \cdot \ln\left(\frac{n_e(x, t)}{N_0}\right) \quad (17)$$

$$E_{fh}(x, t) = E_{VB}(x, t) - k \cdot T \cdot \ln\left(\frac{n_h(x, t)}{N_0}\right) \quad (18)$$

Potential, effective bands and quasi Fermi levels are calculated as post-processing after the simulation.

Further details of the simulation model can be found in our previous publications [58–60].

6.2 MODEL PARAMETERS AND QUANTITIES

Table 1 lists all parameters including the equation they influence and all other quantities occurring in the equations of the previous chapter.

Symbol	Parameter	Unit
d	active layer thickness equation for applied voltage (Eq. 10), boundary hole density (Eq. 4)	nm
N_A	acceptor doping density (p-type) Poisson-equation (Eq. 9)	cm^{-3}
N_D	donor doping density (n-type) Poisson-equation (Eq. 9)	cm^{-3}
μ_e	electron mobility electron drift-diffusion equation (Eq. 6)	$cm^2 \cdot V^{-1} \cdot s^{-1}$
μ_h	hole mobility hole drift-diffusion equation (Eq. 7)	$cm^2 \cdot V^{-1} \cdot s^{-1}$
R_S	cell series resistance equation for applied voltage (Eq. 10)	Ω
S	device surface equation for applied voltage (Eq. 10)	cm^2

table continues on the next page

Symbol	Parameter	Unit
G_{opt}	photon to charge conversion efficiency <i>continuity-equations (Eq. 1 and Eq. 2)</i>	1
B	radiative recombination coefficient <i>continuity-equations (Eq. 1 and Eq. 2) via term for recombination (Eq. 5)</i>	$m^3 \cdot s^{-1}$
ϵ_r	relative electric permittivity <i>Poisson-equation (Eq. 9), equation for the total current (Eq. 8)</i>	1
E_{LUMO}	energy of the lowest unoccupied molecular orbit (LUMO) <i>equation for applied voltage (Eq. 10) via built-in voltage (Eq. 11, Eq. 12)</i>	eV
E_{HOMO}	energy of the highest occupied molecular orbit (HOMO) <i>equation for applied voltage (Eq. 10) via built-in voltage (Eq. 11, Eq. 13)</i>	eV
N_0	density of chargeable sites <i>equation for applied voltage (Eq. 10) via built-in voltage (Eq. 11, Eq. 12, Eq. 13)</i>	cm^{-3}
T	device temperature <i>drift-diffusion equations (Eq. 7, Eq. 6), equation for applied voltage (Eq. 10) via built-in voltage (Eq. 11, Eq. 12, Eq. 13)</i>	K
V_{source}	voltage of the voltage source that is connected to the device <i>equation for applied voltage (Eq. 10)</i>	V
n_{e0}	electron density at the left electrode <i>boundary condition for continuity-equation at $x=0$ (Eq. 1), equation for applied voltage (Eq. 10) via built-in voltage (Eq. 11, Eq. 12)</i>	cm^{-3}
n_{h0}	hole density at the right electrode <i>boundary condition for continuity-equation at $x=d$ (Eq. 2), equation for applied voltage (Eq. 10) via built-in voltage (Eq. 11, Eq. 13)</i>	cm^{-3}
Φ_A	workfunction anode	eV
Φ_C	workfunction cathode	eV
V_{bi}	built-in voltage	V
n_e	electron density	cm^{-3}
n_h	hole density	cm^{-3}
j_e	electron current	$mA \cdot cm^{-2}$
j_h	hole current	$mA \cdot cm^{-2}$
j	total current	$mA \cdot cm^{-2}$

table continues on the next page

Symbol	Parameter	Unit
E	electric field	$V \cdot m^{-1}$
φ	potential	V
R	recombination	$cm^{-3} \cdot s^{-1}$
$g(x)$	absorption profile	$cm^{-3} \cdot s^{-1}$
x	dimension in layer direction	nm
t	time	s
E_{CB}	energy of the conduction band – In comparison with E_{LUMO} this band includes the band bending caused by the electric field.	eV
E_{VB}	energy of the valence band – In comparison with E_{VB} this band includes the band bending caused by the electric field.	eV
E_{fe}	quasi Fermi level of electrons	eV
E_{fh}	quasi Fermi level of holes	eV
ϵ_0	vacuum permittivity	$F \cdot m^{-1}$
q	unit charge	C
k	Boltzmann constant	$J \cdot K^{-1}$

Table 1: Parameter and quantities used in equations in section [Model Equations](#).

6.3 PEROVSKITE SIMULATION MODEL

The simulation scheme used for transient and steady-state simulation is shown in [Figure 14](#). The mesoporous TiO_2 structure where the MALI is infiltrated into is neglected. We model the absorbing layer as one material with one transport level for holes and one for electrons. We assume fast electron transfer to the TiO_2 and electron transport to happen only within the TiO_2 . We explain this assumption in detail in section [Slow Regime \(Milliseconds to Minutes\)](#).

In section [Slow Regime \(Milliseconds to Minutes\)](#) the device is simulated with different distributions of ions. Therefore on each side of the MALI containing layer an additional virtual layer is added with $5nm$ thickness to model the ions close to the interface. This layer is also used to control the surface recombination of charge carriers at the electrodes. For simplicity charge transport in the compact TiO_2 layer and in the Spiro-OMeTAD layer is disregarded. In further research the influence of the mesoporous layer on trap-density, mobility and doping needs to be investigated in more detail. Also the distribution of the ionic species within the perovskite layer is subject of further investigations.

The solar cell structure is simplified for the numerical simulation. Drift-diffusion is calculated within one homogeneous layer neglecting the meso-porous scaffold and the interface layers.

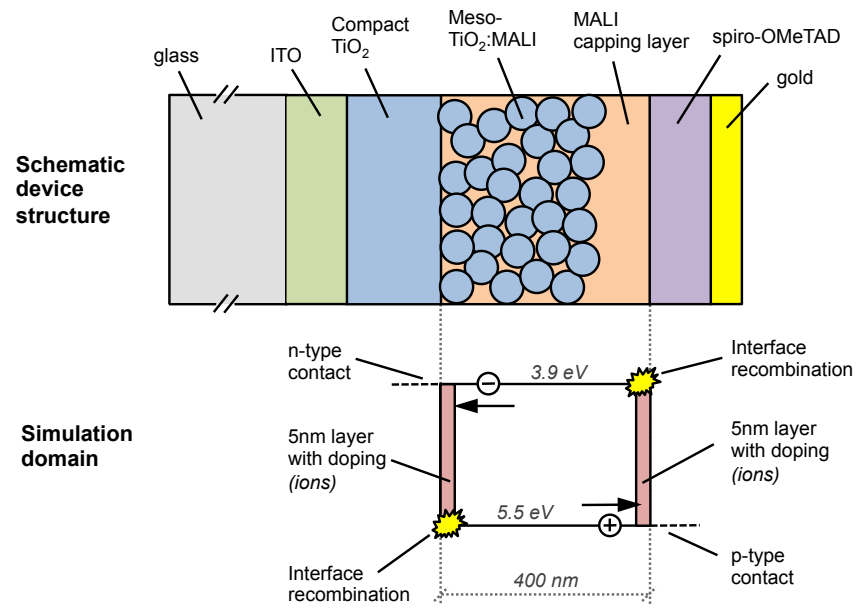


Figure 14: Device structure and simulation domain. The perovskite layer [MALI](#) and the mesoporous TiO_2 is simulated as one effective medium with one electron and one hole transport level.

RC CORRECTION

In this thesis a method to correct [RC effects](#) is applied to correct [photo-CELIV](#) experiment in section [Fast Regime \(Microseconds to Milliseconds\)](#). In this section the extraction of the series resistance and the geometrical capacitance of a device is explained and the derivation of the correction formula ([Equation 55](#)) is shown.

Each device with a dielectric between two electrodes has a capacitance. Changing the voltage V on a capacitance C requires a current i to flow to charge the electrodes.

$$i(t) = C \cdot \frac{dV}{dt} \quad (19)$$

With a resistance R_S in series an RC-circuit is formed with a time constant τ .

$$\tau = R_S \cdot C \quad (20)$$

Physical effects that happen on a time scale shorter than τ will therefore be hidden by [RC effects](#).

A device with a dielectric has a capacitance that forms an RC-circuit with all resistances in series, like contact resistance and measurement resistance.

7.1 DETERMINING SERIES RESISTANCE AND CAPACITANCE

In order to determine the series resistance R_S and the geometrical capacitance C of the solar cell, a voltage step of -0.3 Volt is applied to the device. In reverse direction the device is blocking, so only an RC-current flows charging the capacitance. [Figure 15](#) shows the simple electric circuit used to extract R_S and C_{geom} . Compared to the scheme used to correct for [RC effects](#) ([Figure 17](#) on page 39) the *cell* is omitted as it is considered to be fully blocking in reverse direction.

The geometrical capacitance and the series resistance are determined by applying a small voltage step in reverse direction.

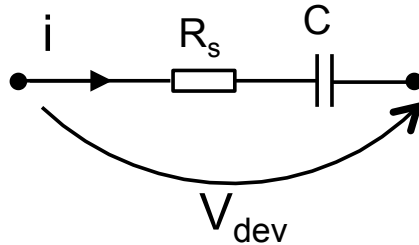


Figure 15: RC-circuit used to fit the measured current.

Equation 21 describes the relation of current and voltage of the circuit in Figure 15. The measured transient voltage $V_{dev}(t)$ is used to calculate the RC-current.

$$\frac{di}{dt} = \frac{1}{R_S} \cdot \frac{dV_{dev}}{dt} - \frac{1}{R_C \cdot C} \cdot i(t) \quad (21)$$

The current of an RC-circuit can be described analytically. Fitting the analytical solution to the measurement allows to extract the capacitance and the series resistance.

Figure 16b shows two voltage steps with different rise-times that are applied to the perovskite solar cell (PSC). A rise-time is used to avoid high current peaks. In Figure 16a the current response to the voltage steps is shown. The series resistance R_S and the capacitance C of Equation 21 are now adjusted such to fit both currents. The result is shown in black using values of $R_S = 59.9 \Omega$ and $C = 10.0 \text{ nF}$.

The RC-fits show more noise than the original current because the RC-fits are calculated using the measured voltage and its derivative.

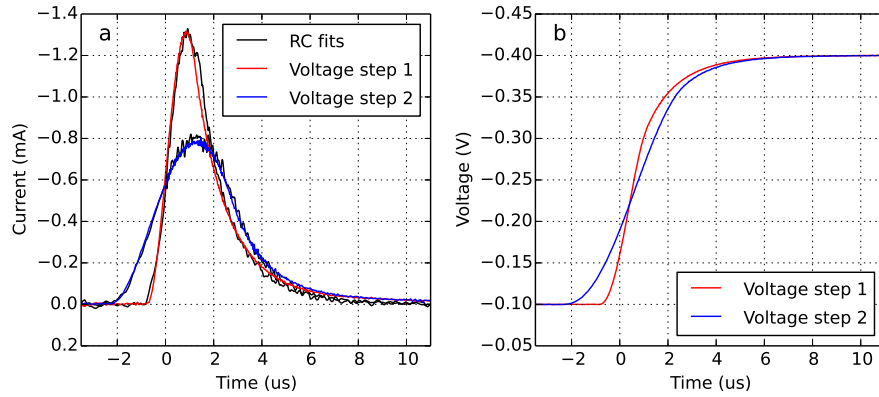


Figure 16: a) Current response to a voltage step. b) applied voltage step with varied rise time.

7.2 DERIVATION OF THE RC-CURRENT CORRECTION

The current of a device with a capacitance and a series resistance can be corrected for the RC-current with the model presented in this section.

In the previous section the series resistance R_S and the geometric capacitance C were determined. These values are now used to calculate the RC-current and correct the device-current. Figure 17 shows the model for the RC-correction. Hereby the measured voltage of the device $V_{dev}(t)$ and its current $i_{dev}(t)$ are used to calculate the current that flows in the cell $i_{cell}(t)$.

The current that flows into the geometric capacitance C_{geom} is

$$i_C(t) = C_{geom} \cdot \frac{dV_C}{dt} \quad (22)$$

with $V_C(t)$ being

$$V_C(t) = V_{dev}(t) - R_S \cdot i_{dev}(t) \quad (23)$$

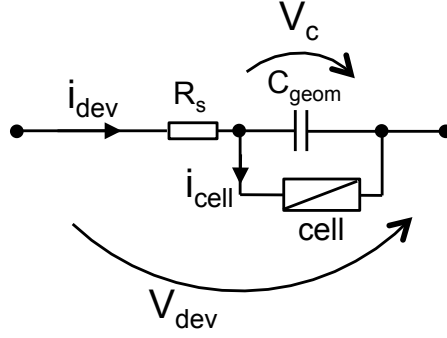


Figure 17: Electrical circuit used to correct the cell current for the RC displacement current. This figure is a reprint of [Figure 31](#)

The current that flows into the capacitance i_C is now subtracted from the device current to obtain the corrected current i_{cell} .

$$i_{cell}(t) = i_{dev}(t) - i_C(t) \quad (24)$$

Filling in [Equation 22](#) and [Equation 23](#) in [Equation 24](#) results in the final formula for the RC-current correction of a device with a geometrical capacitance C_{geom} , a series resistance R_S , a measured device voltage $V_{dev}(t)$ and a measured device current $i_{dev}(t)$.

$$i_{cell}(t) = i_{dev}(t) - C_{geom} \cdot \frac{dV_{dev}}{dt}(t) - R_S \cdot C_{geom} \cdot \frac{di_{dev}}{dt}(t) \quad (25)$$

Using the series resistance R_S , the geometrical capacitance C_{geom} , the measured current $i_{dev}(t)$ and the measured voltage $V_{dev}(t)$ the cell current $i_{cell}(t)$ can be calculated according to [Equation 25](#).

Part III

SOLAR CELL PHYSICS

SOLAR CELL PHYSICS

In this section basic physical principles of solar cells are discussed. Not to overload this section the general introduction to semiconductors explaining holes, doping, bands and absorption as well as the general introduction to optics explaining the sun spectrum and Shockley-Queisser limit are omitted. The focus of this section lies in the charge transport.

Solar cell physics with focus on charge transport is discussed in this chapter.

8.1 GENERAL PRINCIPLE

In all solar cell types an incident photon that is absorbed, leads to an excitation of an electron from the valence band (or HOMO-level) to the conduction band (or LUMO-level). The electron can in this state fall back to the valence band with a probability depending on the possibilities to get rid of its energy via photon- or phonon-emission.

The absorption of a photon leads to the excitation of an electron to a state with higher energy.

The hole in the valence band and the electron in the conduction band attract each other due to coulomb interaction. This bound state of electron and hole can be described as quasi-particle that is called **exciton**. Thermal energy, an electric field or a material interface is required to dissociate an **exciton** into a free electron and a free hole.

The main principle of a solar cell is, that an excited electron leaves the device at high potential doing work on an external load and recombining with the hole on low potential.

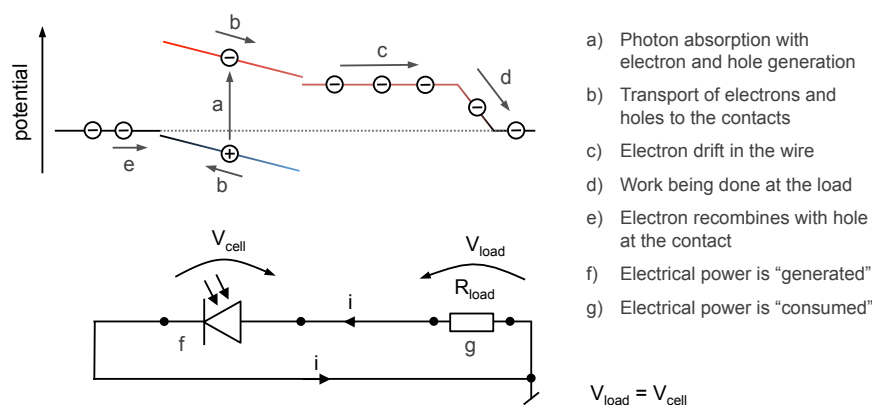


Figure 18: General working principle of a solar cell illustrated with an extended band diagram (upper graph) and an electric circuit including a load (lower graph). Please note that the current i is defined positive, resulting in electrons moving in the opposite direction.

Figure 18 shows the main operation principle of a solar cell. In step a light is absorbed and the **exciton** separated as described above. According to the driving forces explained in the next section the electrons and holes move to the contacts (step b). The wire connected to the solar cell is metallic and has therefore many free electrons trans-

porting the charge (step *c*). In step *d* the electron performs work on the load by going from the high potential to the low potential. In this illustration the cell is at its maximum power point (MPP) somewhere between the short-circuit current and the open-circuit voltage. To reach this state the load R_{load} must be chosen respectively.

In the electric circuit in Figure 18 the voltage of the solar cell V_{cell} is in the opposite direction as the current i (see *f*). From an electrical point of view in the solar cell power is generated whereas in the load resistor R_{load} the power is dissipated (see *g*).

8.2 DRIVING FORCES AND BAND DIAGRAMS

The gradient of the Fermi level is the driving force for electrons and holes and includes drift and diffusion.

The driving force for electrons and holes is the gradient of the Fermi level [61]. The total particle currents j_e and j_h are described in Equation 26 and 27.

$$j_e = n_e \cdot \mu_e \cdot \text{grad}(E_{fe}) \quad (26)$$

$$j_h = -n_h \cdot \mu_h \cdot \text{grad}(E_{fh}) \quad (27)$$

where n_e and n_h are the electron and hole densities, μ_e and μ_h are the electron and hole mobilities and E_{fe} and E_{fh} are the Fermi levels for electrons and holes, respectively.

The Fermi level is equal to the electro-chemical potential¹ η that consists of the electrical potential φ and the chemical potential γ as shown in Equation 28 and 29.

$$E_{fe} = \eta_e = \gamma_e + q \cdot \varphi \quad (28)$$

$$E_{fh} = -\eta_h = -\gamma_h - q \cdot \varphi \quad (29)$$

The chemical potential of electrons and holes (γ_e and γ_h) is dependent on their charge carrier density (n_e and n_h) according to Equation 30 and 31,

The chemical potential depends logarithmically on the charge carrier density.

$$\gamma_e = -\chi_e + k \cdot T \cdot \ln\left(\frac{n_e}{N_C}\right) \quad (30)$$

$$\gamma_h = -\chi_h + k \cdot T \cdot \ln\left(\frac{n_h}{N_V}\right) \quad (31)$$

where χ_e is the electron affinity, χ_h the ionization potential, N_C and N_V is the effective density of states, k is the Boltzmann constant and T is the temperature.

Combining Equation 26, 28 and 30 results in Equation 32 for electrons. Replacing the gradient with a one dimensional derivative finally results in Equation 34 - the well-known drift-diffusion equation as described in chapter SIMULATION MODEL in Equation 6.

¹ The electro-chemical potential is in contrast to its name not a potential but an energy.

$$j_e = n_e \cdot \mu_e \cdot \text{grad} \left(-\chi_e + k \cdot T \cdot \ln \left(\frac{n_e}{N_C} \right) + q \cdot \varphi \right) \quad (32)$$

$$j_e = n_e \cdot \mu_e \cdot k \cdot T \cdot \frac{\partial}{\partial x} \left(\ln \left(\frac{n_e}{N_C} \right) \right) + n_e \cdot \mu_e \cdot q \cdot \frac{\partial \varphi}{\partial x} \quad (33)$$

$$j_e = \mu_e \cdot k \cdot T \cdot \frac{\partial n_e}{\partial x} + n_e \cdot \mu_e \cdot q \cdot \frac{\partial \varphi}{\partial x} \quad (34)$$

The result for the equation for holes is shown in Equation 35.

$$j_h = \mu_h \cdot k \cdot T \cdot \frac{\partial n_h}{\partial x} - n_h \cdot \mu_h \cdot q \cdot \frac{\partial \varphi}{\partial x} \quad (35)$$

To make the long story short: The gradient of the **Fermi level** is the driving force for the charge carriers combining forces of diffusion (chemical potential) and forces of drift (electrical potential). In solar cell physics the **Fermi levels** and band structures are often illustrated to understand the device operating mechanisms. Band structures are explained in the next section.

*Inserting the equations of the **Fermi level** into the equation defining the current, results exactly in the drift-diffusion equation used in the numerical simulation.*

8.3 BAND DIAGRAMS AND BASIC SOLAR CELL OPERATION

To understand band structures we look at a simple solar cell with good charge transport, low recombination and a built-in voltage that drives the charge carriers to the electrodes. The device is not doped and has no traps. The **IV curves** of such an idealised device is shown in Figure 19a.

In a band diagram the energy is plotted versus the position in the layer. In our case the device is illuminated from the left. On the left at $x = 0$ is the anode where the holes are extracted. On the right at $x = 100 \text{ nm}$ is the cathode where the electrons are extracted.

In a general view one can say electrons tend to go up and holes go down.

*A band diagram is the illustration of the effective bands with the two quasi **Fermi levels** and is often used to explain solar cell physics.*

At **short-circuit in the dark** in Figure 19b no current flows. The gradient of the **Fermi level** is zero. The Fermi-level for electrons and holes coincides. The bands are inclined meaning a constant electric field throughout the device.

Under **illumination at short-circuit** in Figure 19c the absorbed photons lead to a Fermi-level splitting. There is no voltage drop on the cell. The two contacts (indicated with thick lines) have the same potential. As there is a gradient in both Fermi-levels an electron and a hole current flows.

*The illumination causes a **Fermi level** splitting.*

At an **applied forward voltage in the dark** in Figure 19d the internal field is compensated and the bands become flat. The difference between the Fermi-level of holes on the left and the Fermi-level of electrons on the right is the applied voltage at the device. A forward

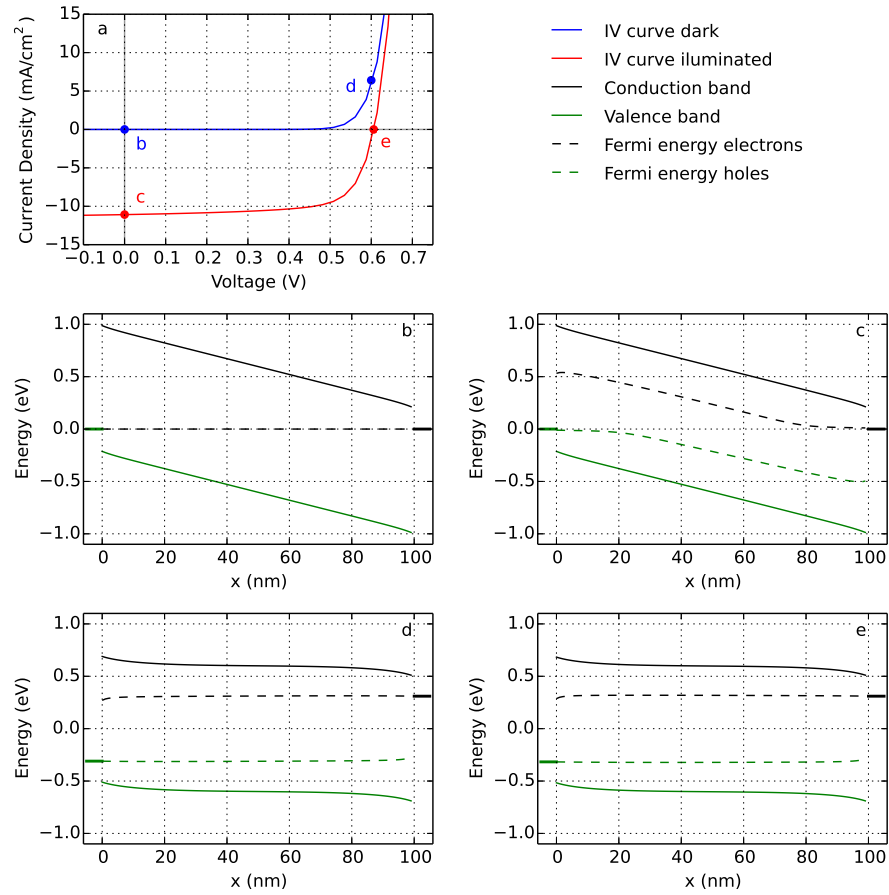


Figure 19: a) Simulated **IV curve** in the dark and illuminated. b) Band diagram at zero volt in the dark. c) Band diagram at zero volt illuminated. d) Band diagram with forward voltage in the dark. e) Band diagram at open-circuit voltage.

current flows. As the charge carrier density is very high, a very small gradient in the Fermi-levels is sufficient to drive the charges.

At **open-circuit** under illumination in **Figure 19e** no current flows - all charges recombine. The charge carrier density is high. This can be seen in the band diagram because the Fermi-levels are much closer to the bands as in case c.

Please note: The total current consisting of electron, hole and displacement current is always constant in x throughout the whole electric circuit (Kirchhoff's law).

8.4 MAJORITY VERSUS MINORITY CARRIER DEVICES

This section categorizes solar cells into majority- and minority-carrier devices.

Solar cells can be categorised in many aspects. In this section the distinction is made between the main driving forces into *minority carrier devices* governed by diffusion and *majority carrier devices* governed by drift. This distinction may be uncommon to many solar cell special-

ists as they only deal with one or the other type. Nevertheless, this distinction is helpful to understand the physics of perovskite solar cells (PSCs).

Figure 20 shows a comparison of the two device types. The majority carrier device is shown as *pin*-structure², the minority carrier device with the same structure but the intrinsic region *i* replaced with n-type doping. Both band diagrams are shown at zero volt under illumination. Charge carriers are created homogeneously throughout the device.

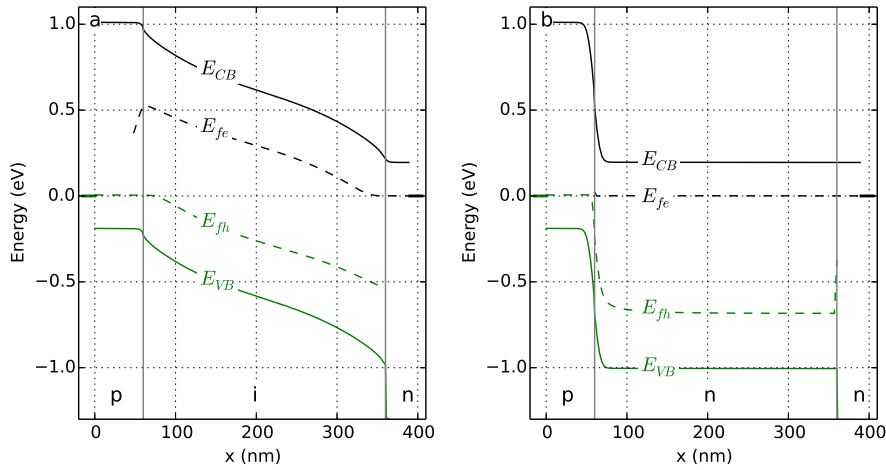


Figure 20: a) Majority carrier device in *pin*-structure. Steep bands indicate a high electric field. b) Minority carrier device in *pn*-structure. Within the device the bands are flat.

8.4.1 Minority Carrier Devices

Minority carrier devices are doped³ what leads to an imbalance of charge carriers in a large part of the device. The transport is limited by the diffusion of the minority carriers.

An example of the band structure in a minority carrier device is shown in Figure 20b. At the *pn*-junction the electric field is very high, whereas in the n-type region it is screened (close to zero). In the n-type region the electron Fermi level (E_{fe}) is much closer to the conduction band (E_{CB}) than the hole Fermi-level (E_{fh}) to the valence band (E_{VB}). This shows that fewer holes are present than electrons. In this example the minority carriers are the holes that need to diffuse from the n-type region to the p-contact. Transport by drift is negligible. The electron transport is not limiting due to the high density.

A majority carrier device is not doped and both charge carrier types have a similar density. In a minority carrier device one charge carrier type is dominant (ex: due to doping) and the other type is in the minority.

*The classical *pn*-junction is a good example of a minority carrier device. The potential mainly drops at the junction, the rest of the device is field-free.*

² The *pin* stands for p-type doped, intrinsic (undoped) and n-type doped.

³ As described in this thesis also traps can lead to a high charge carrier imbalance. Furthermore also a high difference in electron and hole mobility can lead to a high imbalance of charge carriers resulting in a minority carrier device working mechanism.

Most commonly known solar cell technologies are minority carrier devices using a **pn-junction**: crystalline silicon, CdTe, CIGS.

8.4.2 Majority Carrier Devices

Majority carrier devices are not doped and have an therefore an electric field that drives charges.

Majority carrier devices are not doped and therefore the densities of electrons and holes are in a similar order of magnitude. In the majority carrier device shown in **Figure 20a** an electric field is created in the intrinsic region due to the charges of the n-type and p-type region. Alternatively such a field can be created using metals with different **workfunctions** as contacts.

*Please note that also minority carrier devices have a built-in potential. But this potential drops at the **pn-junction**, the rest of the device is field-free.*

In majority carrier devices the diffusion length is often too short such that an electric field is required to transport charge carriers to the electrodes. Common majority carrier devices are amorphous silicon and organic solar cells (**OSCs**).

8.4.3 Lifetime

The lifetime is inversely proportional to the recombination. In minority carrier devices the lifetime defines how long a minority carrier "lives" in average before it recombines.

In *minority carrier devices* the charge carrier lifetime τ is defined as

$$\tau_e = \frac{n_e}{R} \quad (36)$$

where R is the recombination and n is the charge carrier density of the minority. For radiative recombination $R = \beta \cdot n_e \cdot n_h$ the lifetime is independent of the minority carrier density. Assuming a p-doped device ($n_h = N_A$) the lifetime results in

$$\tau_e = \frac{n_e}{\beta \cdot n_e \cdot n_h} = \frac{1}{\beta \cdot N_A} \quad (37)$$

where β is the recombination prefactor, n_h is the hole density and N_A is the doping density. Assuming $n_h \gg n_e$ (which is the case in a doped device) the hole density is unaffected by the recombination and can be considered as constant. Therefore the charge carrier lifetime can be considered as a constant material parameter.

Knowing the diffusion constant D the diffusion length L_D can be calculated according to

$$L_D = \sqrt{D_e \cdot \tau_e} = \sqrt{\mu_e \cdot k \cdot T \cdot \tau_e} = \sqrt{\frac{\mu_e \cdot k \cdot T}{\beta \cdot N_A}} \quad (38)$$

Also the minority carrier diffusion length can be regarded as constant material parameter if the material is doped. For an efficient device

The diffusion length defines how far a charge carrier can diffuse in average.

the diffusion length needs to be significantly larger than the device thickness.

In *majority carrier devices* the concept of charge carrier lifetime cannot be applied directly. It cannot be assumed that a majority carrier density is constant and the lifetime of the minority carriers is limiting. Both the electron lifetime τ_e and the lifetime of holes τ_h depend on each other as shown in Equation 39.

$$\tau_e(n_h) = \frac{1}{\beta \cdot n_h} \quad \tau_h(n_e) = \frac{1}{\beta \cdot n_e} \quad (39)$$

Both the electron density n_e and the hole density n_h can vary over orders of magnitude depending on the position in the device and depending on time. Charge carrier lifetime can therefore not be regarded as constant material parameter in a majority carrier device like an OSC. Consequently the product of diffusion constant D and lifetime τ as shown in Equation 38 is not physically meaningful. A charge carrier travelling through the device will have different lifetimes depending on its position. Furthermore, in these types of devices charge carriers are mainly transported by drift.

Although the physical meaning is questionable the mobility-lifetime-product is sometimes used in publications about majority carrier devices like OSCs [62, 63].

8.4.4 Traps and Doping

The doping of a semiconductor can be intentional like in the case of a silicon solar cell or unintentional, as sometimes the case in organic photovoltaics. In the second case it is detrimental to device performance since the electric field is screened and charges cannot be transported to the electrodes as shown by Kirchartz et al.[64].

Doping usually refers to the creation of free charge carriers leaving an ionized core of opposite charge polarity activated at room temperature. Figure 21a and 21c illustrate this process. An atom or molecule is placed in a semiconductor such that the atom's occupied energy level is close to the unoccupied conduction band of the semiconductor. Thermal energy at room temperature is sufficient to ionize this atom or molecule. As shown in Figure 21c a free electron leaves behind an immobile positive charge (hole).

Charge trapping can however lead to the same effect what is sometimes referred to as photo-doping [65]. Figure 21b shows a semiconductor with an additional energy level somewhere in the band-gap acting as hole-trap. Without any activation it is neutral as in the case of Figure 21a.

The concept of lifetime is not physically meaningful for majority carrier devices. It is not constant in time and space due to similar charge carrier densities.

The doping of a semiconductor results in additional free charge carriers and somehow fixed charges (ionic cores) of the other charge polarity.

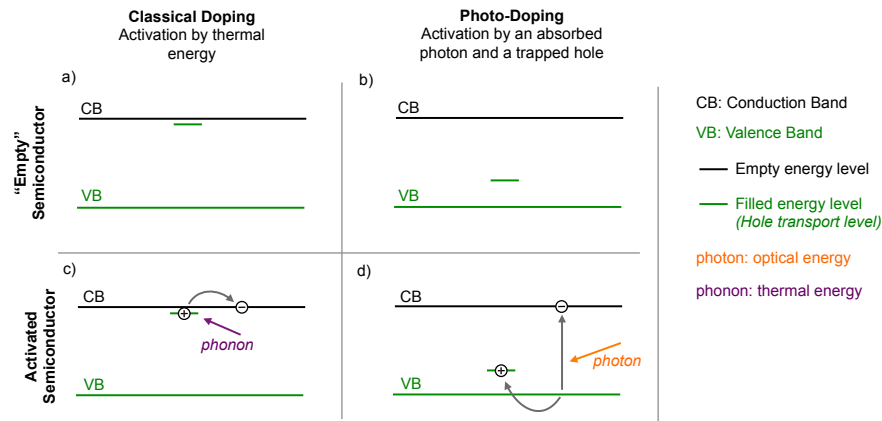


Figure 21: a) An "empty" semiconductor containing a filled energy level close to the conduction band. b) An "empty" semiconductor containing a filled energy level somewhere in the band-gap (this is also called a hole-trap). c) By thermal energy the electron is moved from its energy level to the conduction band (ionized dopant). d) An electron and a hole are created by photon-absorption. After a while the hole gets trapped (photo-doping).

If a photon is absorbed a free electron and a free hole are created. If the hole falls into the hole-trap it is immobile. The two situations (classical doping and photo-doping) lead to the same result.

In numerical drift-diffusion modelling doping is added as fixed charge in the Poisson equation as shown in [Equation 9](#) in Section 6. The condition of charge balance automatically leads to additional free charge carriers of the same amount.

8.5 RECOMBINATION AND OPEN-CIRCUIT VOLTAGE

Recombination is the annihilation of an electron and a hole. The potential energy of the electron in the conduction band thereby needs to be transferred elsewhere - in [phonon](#) and/or photon emission. [Figure 22](#) shows the four recombination types that can be present in semiconductors.

Radiative recombination is physically inherent in absorbing materials, meaning it is the recombination type that cannot be avoided. In the dark at thermal equilibrium all rates of generation are equal to the rates of recombination - this is the principle of *detailed balance* [61]. The probability of an electron and a hole finding each other increases with both densities. Therefore the recombination rate is proportional

If traps get filled they can have a very similar effect like classical doping - Often this is referred to as photo-doping.

In radiative recombination a photon is emitted. It is usually the weakest form of recombination. It can be directly determined by measuring the electroluminescence (EL)-signal at forward bias.

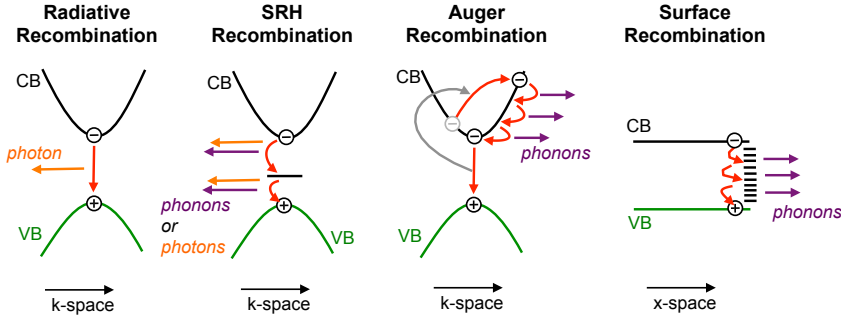


Figure 22: Schematic illustration of recombination types in semiconductors.

to both charge carrier densities and consequently depends on the [Fermi level](#) splitting as shown in [Equation 40](#).

$$R_{rad} = \beta \cdot n_e \cdot n_h = \beta \cdot e^{\frac{E_{fe} - E_{fh}}{k \cdot T}} \quad (40)$$

As indicated in [Figure 22](#) a photon is emitted in radiative recombination. The radiative recombination can therefore directly be determined by measuring the [EL-signal](#).

Generally one can say that a good solar cell with a high open-circuit voltage shows also a high [EL-signal](#). Radiative recombination is generally weaker than other forms of recombination. A high [EL-signal](#) therefore indicates that all other recombination types are not dominant leading to a high charge carrier density and a high open-circuit voltage.

Shockley-Read-Hall (SRH) recombination (also known as trap-assisted recombination) requires an intermediate energy level within the band-gap. The energy is either emitted by a [phonon](#) or a photon as shown in [Figure 22](#). Such mid-gap states occur by [dangling bonds](#) of a crystal or by impurities. In a perfect material [SRH](#) recombination is absent.

Trap assisted recombination is a two-stage process requiring an energy level within the band-gap.

Its mathematical description is more complex than for radiative recombination. For a cell in steady-state the [SRH](#) recombination is described as

$$R_{SRH} = n_{imp} \cdot \frac{n_e \cdot n_h - n_i^2}{\frac{n_e + N_C \cdot e^{-\frac{E_{CB} - E_{imp}}{k \cdot T}}}{c_h} + \frac{n_h + N_V \cdot e^{-\frac{E_{imp} - E_{VC}}{k \cdot T}}}{c_e}} \quad (41)$$

where n_{imp} is the density of states of the impurities, n_i is the intrinsic density, E_{imp} is the energy level of the impurity, c_h and c_e are the capture rates of electrons and holes and N_C and N_V are the effective density of states of the conduction band and valence bands, respectively.

Auger recombination is only relevant for high charge carrier densities in minority carrier devices.

Auger recombination can be regarded as the reverse of impact ionization. An electron transfers its energy to another electron that is moved up to a higher state in the conduction band. The second electron afterwards thermalises down to the conduction band edge by emitting **phonons** as shown in [Figure 22](#). [Equation 42](#) describes the Auger recombination for electrons and holes

$$R_{Aug,e} = C_e \cdot n_e^2 \cdot n_h \quad R_{Aug,h} = C_h \cdot n_e \cdot n_h^2 \quad (42)$$

where C_e and C_h are Auger recombination constants. As Auger recombination scales with the cube of the charge carrier density, it is large for devices with high doping. It is practically irrelevant for majority carrier devices. In silicon solar cells it largely determines the efficiency limits of the record devices [\[61\]](#).

Surfaces contain many defects that create states within the band-gap, leading to higher recombination at the surface.

Surface recombination happens via one or more states that are present at the surface of an interface to another material. In crystals surfaces always contain **dangling bonds** or defects that create states within the band-gap. A charge carrier reaching a surface hops from state to state losing its energy by **phonon** emission as shown in [Figure 22](#). Surface recombination is described as

$$R_{Sur,e} = \nu_e \cdot n_e \quad R_{Sur,h} = \nu_h \cdot n_h \quad (43)$$

where ν is the surface recombination velocity.

Please note: The expression surface recombination is used to describe the detrimental recombination of charge carriers at the opposite electrode - not the charge extraction. Holes recombine at the electron contact, electrons at the hole contact.

Metals are considered to have an infinite surface recombination velocity ν , meaning that all charge carriers of the wrong type reaching the surface are 'immediately' lost.

The term surface passivation means applying measures to lower the surface recombination velocity. This can be done by coating additional buffer layers that are blocking one charge carrier type or by additional local doping at the contact⁴.

Surface passivation is required for minority-carrier devices to reach charge selectivity.

Minority carrier devices require passivated⁵ surfaces as charges would run into the opposite electrode. We name this *charge selectivity*. In majority carrier devices charge selectivity is ensured by the

⁴ In silicon solar cells this concept is called back surface field BSF. The p-type wafer is doped with p+ at the contact to reduce the electron concentration and passivate the surface.

⁵ A passivated surface has only few mid-gap levels leading to a low surface recombination.

electric field. Surface passivation is therefore less detrimental in these devices.

8.5.1 Recombination Order

The recombination order provides information about the dominant recombination type. The recombination order is a simplified view on the cell as the charge carrier concentration is zero-dimensional and similar electron and hole densities are assumed. The recombination order k is defined as

$$R = n^k \quad (44)$$

where R is the recombination and n is the charge carrier density.

Assuming the simplification $n = n_e = n_h$ the radiative recombination can be simplified to:

$$R_{rad} = \beta \cdot n_e \cdot n_h = \beta \cdot n^2 \quad (45)$$

The recombination order for radiative recombination is therefore 2. For SRH recombination the recombination order results in 1 as shown in Equation 46. For the Auger recombination the recombination order is 3 as shown in Equation 47.

$$R_{SRH} = n_{imp} \cdot \frac{n_e \cdot n_h}{C_1 \cdot n_e + C_2 \cdot n_h + C_3} = C_4 \cdot n \quad (46)$$

$$R_{Aug,e} = C_e \cdot n_e^2 \cdot n_h = C_e \cdot n^3 \quad (47)$$

8.5.2 Ideality Factor

The ideality factor⁶ has the same purpose as the recombination order, that is to distinguish recombination types. In this section the relation between ideality factor and recombination order is shown.

The ideality factor n_{id} is used in the equation to describe an IV curve analytically

$$j(V) = j_s \cdot \left(\exp\left(\frac{V \cdot q}{k_B \cdot T \cdot n_{id}}\right) - 1 \right) - j_{ill} \quad (48)$$

⁶ There are two kinds of ideality factors that can differ from each other. The dark ideality factor is measured in the IV-curve forward direction in the dark. The light ideality factor is determined at the slope of the open-circuit voltage versus the light intensity. In this thesis only the second type is treated.

The recombination order is often measured to analyse the dominant recombination type.

The recombination order for radiative recombination or bimolecular recombination is 2.

The recombination order for SRH recombination is 1.

The recombination order for Auger recombination is 3.

The ideality factor is directly related with the recombination order.

The IV curve of a solar cell can be described analytically using the ideality factor.

where j_s is the reverse saturation current and j_{ill} is the current due to illumination. If the ideality factor n_{id} is one, the cell is *ideal* and at its optimum. The 'ideal' ideality factor is always larger than one⁷.

The slope of V_{OC} is measured to determine the ideality factor.

The ideality factor can be determined by analysing the slope of the open circuit voltage versus the logarithmic light intensity. The open-circuit voltage is the difference of the [Fermi level](#) at the contacts. Using [Equation 28](#) and [29](#) this results in [Equation 49](#) for the open-circuit voltage.

$$V_{OC} = \frac{E_{BG}}{q} + \frac{k_B \cdot T}{q} \ln\left(\frac{n_e \cdot n_h}{N_C \cdot N_V}\right) \quad (49)$$

Applying the same simplifications as used in the previous section $n = n_e = n_h$ and substituting all constants with C results in [Equation 50](#).

$$V_{OC} = C + \frac{k_B \cdot T}{q} \ln(n^2) \quad (50)$$

At open-circuit the recombination R of charge carriers equals the generation G since no current can flow.

$$G = R = n^k \quad (51)$$

Putting [Equation 51](#) into [Equation 50](#) results in

V_{OC} depends logarithmically on the light intensity.

$$V_{OC} = C + \frac{k_B \cdot T}{q} \ln\left(G^{\frac{2}{k}}\right) = C + \frac{k_B \cdot T}{q} \cdot \frac{2}{k} \cdot \ln(G) \quad (52)$$

This result shows that the open-circuit voltage depends logarithmically on the charge carrier generation and therefore the light intensity.

Solving the equation that describes the [IV curve](#) ([Equation 48](#)) for $j(V) = 0$ results in [Equation 53](#).

$$V_{OC} = n_{id} \cdot \frac{k_B \cdot T}{q} \cdot \ln\left(1 + \frac{j_{ill}}{j_s}\right) \quad (53)$$

As the short circuit current is much larger than the saturation current ($j_{ill} \gg j_s$) the expression $1 + j_{ill}/j_s$ can be regarded as proportional to the generation G . This leads to the relation

$$n_{id} = \frac{2}{k} = \frac{dV_{OC}}{d(\ln(G))} \cdot \frac{q}{k_B \cdot T} \quad (54)$$

Relation between ideality factor and recombination order.

⁷ This however is the theory. Further below we will see that this is not always the case.

With pure radiative recombination the recombination order is 2 and the ideality factor is 1. If SRH recombination is dominant the recombination order is 1 and the ideality factor is 2.

To understand the applicability and limitations of the ideality factor numerical simulations are performed. Figure 23a shows simulated open-circuit voltage versus light intensity with varied radiative recombination efficiency⁸. A device without doping, traps and with well passivated contacts is simulated such that radiative recombination is the only relevant recombination. The open-circuit voltage is therefore exactly proportional to the logarithm of the light intensity. The ideality factor calculated from Equation 54 is exactly 1 as shown in Figure 23c.

If radiative recombination is dominant the V_{OC} versus light intensity is exactly logarithmic in the simulation.

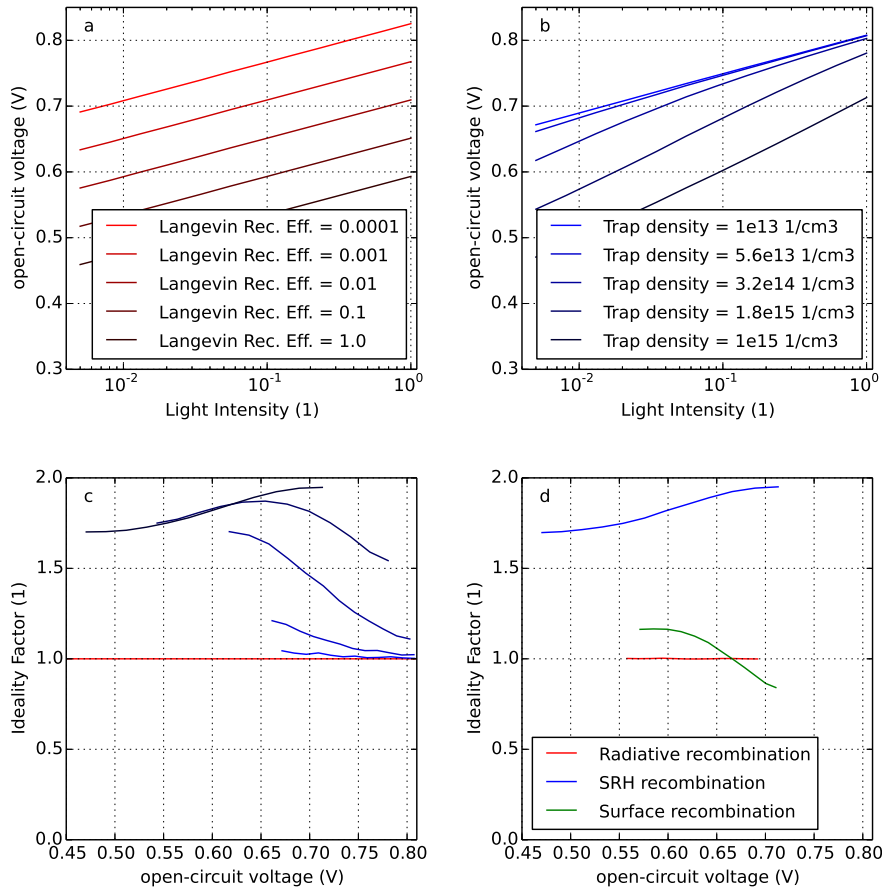


Figure 23: a) Simulated open-circuit voltage with varied radiative recombination efficiencies. b) Simulated open-circuit voltage with SRH recombination and varied trap-density. c) Simulated ideality factors for the radiative recombinations and the SRH recombinations of a and b. d) Simulated ideality factors for different recombination types.

⁸ In this model Langevin recombination is used, that is proportional to radiative recombination efficiency.

SRH recombination in comparison has a different slope (open-circuit voltage versus logarithmic light intensity) with varying trap density (Figure 23b). The ideality factor changes between one and two depending on the light intensity as shown in Figure 23c.

*With
SRH-recombination
the simulated
ideality factor varied
between 1 and 2
depending on the
light intensity.*

Figure 23d compares the ideality factors of radiative recombination, SRH recombination and surface recombination. In this example the ideality factor of the simulation with surface recombination gets even below one.

The concept of recombination order and ideality factor is strongly simplified. Due to spatial variation of charge carrier density, variation in energy levels or variation in charge carrier mobilities the ideality factor can reach values below one or above three [66]. Conclusions from ideality factors should therefore be made carefully.

Part IV

RESULTS AND DISCUSSION

RESULTS

In this thesis methylammonium lead iodide (MALI) perovskite solar cell (PSC) with mesoporous TiO_2 scaffold and Spiro-OMeTAD are investigated. More details about the device can be found in chapter [DEVICE FABRICATION](#).

9.1 IV CURVE HYSTERESIS

The shape of an [IV curve](#) of a perovskite solar cell can vary depending on voltage ramp speed and direction [30, 31, 46]. Though hysteresis effects have been observed and discussed at length, their origin is still subject of intense debate. Unger et al. showed that hysteresis effects are related to slow processes that occur on the same time scale as the voltage ramps used [31]. We shine light on this puzzle by systematic IV curve acquisitions with voltage pulses and with pre-bias voltage.

Perovskite solar cells very often show a hysteresis when the [IV curve](#) is measured upward or downwards.

The solar cells we investigate have generally a small hysteresis. For this study about charge transport dynamics and slow effects we chose a batch with a stronger hysteresis. The cell investigated has a [PCE](#) of about 12%.

The investigated cell has an efficiency of 12%.

[Figure 24a](#) shows the [IV curve](#) hysteresis measured with a slow sinusoidal voltage with 10 Hz and 0.1 Hz. This results in a measurement time of 100 milliseconds and 10 seconds, respectively. *Please note that this hysteresis measurement was not performed under AM1.5 but with an illumination from a high-power white LED.* The cycle going from high voltage to low voltages results in a higher open-circuit voltage and higher fill factor. The physical origin of this effect will be addressed further below in this thesis.

The shape of the [IV curve](#) depends on the slope speed and direction. Going from high to low voltage results in a higher fill factor.

[Figure 24b](#) shows the external quantum efficiency ([EQE](#)) of the investigated [PSC](#).

9.2 TRANSIENT CURRENT RESPONSE FROM MICROSECONDS TO MINUTES

To gain knowledge about the origins of the hysteresis it is promising to perform transient experiments as they provide valuable information about charge transport and related processes such as recombination and trapping. Thus, on [PSC](#) transient electroluminescence ([TEL](#)) [46], transient photo-voltage ([TPV](#)) [67, 68, 46], photo-generated charge extraction by linearly increasing voltage ([photo-CELIV](#)) [69, 70], transient photocurrent ([TPC](#)) [46] and

Transient measurements provide important information about the dynamics of physical processes.

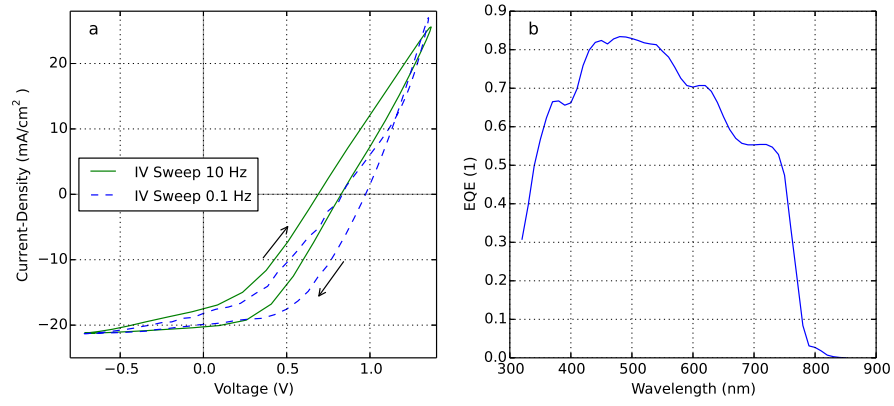


Figure 24: a) Current-voltage characteristics measured with a sinusoidal voltage with frequency 10 Hz and 0.1 Hz under illumination. b) EQE measurement of the PSC investigated.

transient photo-conductivity [32] have been measured. Except for the TPV measurements of Baumann et al. [67] so far all transient experiments were reported with only two or three orders of magnitude in time – either in the regime of milliseconds or seconds.

The transient photocurrent (TPC) of the perovskite solar cell increases over 8 orders of magnitude in time and reaches steady-state only after 5 minutes.

Extraordinary slow effects occur under illumination and in the dark.

Slow transient effects are also present during the TPV rise.

We perform transient measurements with a broad dynamic range. Figure 25a shows the transient photocurrent of a perovskite solar cell as a response to a light step (light is turned on at $t = 0$, $V = 0$). At 4 microseconds the current overshoots and is followed by a steady rise over 8 orders of magnitude in time lasting up to 5 minutes. This long rise is extraordinary. We have previously investigated microcrystalline silicon solar cells, CdTe, CIGS, various OSC, hybrid and DSSC. In all these devices the current rise takes place on very different time scales but always ends within two or three orders of magnitude in time (for example $0.1 \mu\text{s}$ to $10 \mu\text{s}$, or $1 \mu\text{s}$ to $100 \mu\text{s}$).

In Figure 25b the current response to a voltage step in the dark (voltage is turned on at $t = 0$) is shown. The initial current peak (up to $10 \mu\text{s}$) is a RC displacement current charging the geometrical capacitance as we have confirmed by independent determination of the series resistance and capacitance (see Section Determining series resistance and capacitance). After the RC peak the current is slightly decreasing and starts to rise again only after 10 milliseconds. From Figure 25 we conclude that slow effects on different time scales occur under illumination and in the dark.

Figure 26a shows transient photovoltage for light intensities of 1%, 10% and 100%. Also here a dynamic range covering 8 orders of magnitude in time is observed.

Figure 26b compares different methods for charge carrier density determination plotted versus the illumination time. In the charge extraction technique the device is illuminated and kept at open-circuit. After light turn-off the voltage is switched to zero. To get the num-

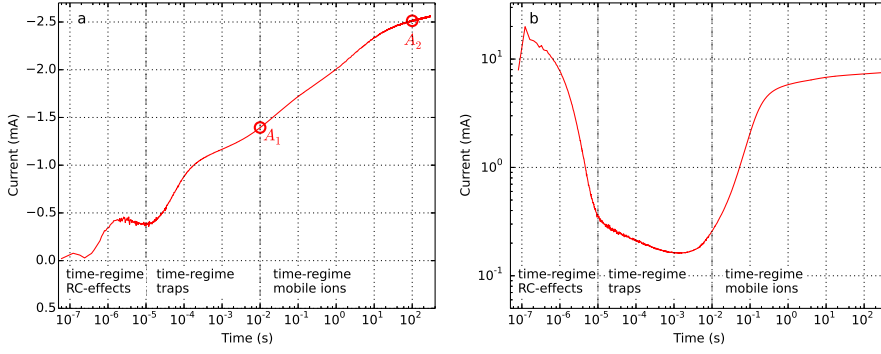


Figure 25: a) transient photocurrent (TPC) measurement of a perovskite solar cell. The LED light is turned on at $t = 0$ with an intensity of approximately one sun. The applied voltage is $V(t) = 0$ V. A_1 and A_2 mark two states of the solar cell that are referred to later in Figure 27. b) Current response to a voltage step in the dark with $V = 2$ V. The first regime is governed by RC effects, the second by space charge effects due to imbalanced charge mobilities and traps. The third regime is governed by mobile ions.

ber of extracted charges the current is integrated. The photo-CELIV experiment is explained in section Fast Regime (Microseconds to Milliseconds). Here the CELIV current is RC-corrected and integrated to obtain the charge carrier density. These two techniques keep the device at open-circuit before charge extraction. The extracted values are well comparable.

In the technique TPC decay integration a transient photocurrent is measured at short-circuit. After light turn-off the current is integrated to obtain the charge carrier density at short-circuit. For all three charge extraction techniques a steady rise is observed for short illumination durations. This can be explained by the filling of traps. At one millisecond there is a certain saturation until 100 milliseconds. Then the extracted charge of charge extraction and TPC decay integration increase drastically up to almost 10^{18} cm^{-3} . It has been speculated that a change in the ion distribution inside the cell can explain this extraordinarily high charge density of the charge extraction [71]. The origin for this slow rise is subject to further investigations.

In this thesis three different mechanisms are postulated to be present. In the first time regime RC effects dominate, in the second imbalanced mobilities and charge trapping. In the third regime mobile ions changing the electric field influence the total charge current. We put our focus on the second and third regime. In section Slow Regime (Milliseconds to Minutes) we show IV curves with 10 millisecond and 100 second pulses. In section Fast Regime (Microseconds to Milliseconds) we discuss photo-CELIV experiments (up to 10 ms).

The charge carrier density is measured with three techniques depending on the illumination duration. After 1 s illumination the charge density gets unrealistically high - mobile ions may be the origin of this effect.

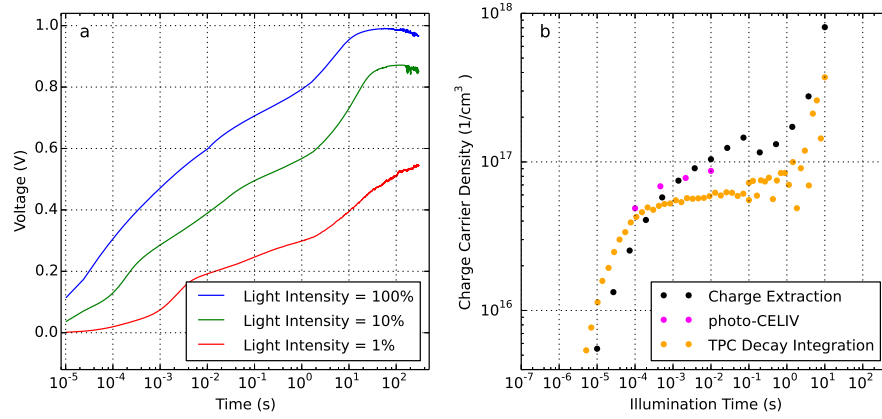


Figure 26: a) transient photo-voltage (TPV) rise for three different light intensities. b) Three different methods to extract the charge carrier density dependent on the illumination duration.

9.3 SLOW REGIME (MILLISECONDS TO MINUTES)

IV curves are measured with voltage and light pulses - once with long and once with short pulse length.

The *slow* effects (ranging from 10 ms to 100 s) are investigated by measuring *IV curve* with rectangular voltage pulses where light and voltage are switched on simultaneously. The current value is read out at the end of the pulse. Measuring *IV curves* with pulsed voltages has the advantage that every voltage point is acquired with exactly the same time after light and voltage turn-on. Between the pulses we wait 20 seconds to give the device sufficient time to recover. Effects on different times scales can be isolated with this approach by choosing different pulse durations. Pulsed *IV curves* are shown in Figure 27a in dots with 10 millisecond and 100 second pulse-length. Each point represents a measurement with one pulse. The *IV curve* acquired with pulse-lengths of 10 milliseconds differs substantially from the one with pulses of 100 seconds duration. Tress et al. [46] postulated that the charge transport properties of these perovskite solar cells depend on the *state* in which the device is. This *state* changes with the applied voltage. In the pulsed *IV curve* with 100 seconds pulse duration the device has time to change to the respective equilibrium *state*. For clarity the short-circuit current after 10 ms and 100 s are marked as state A_1 and A_2 in Figure 27a and Figure 25a.

The cell current depends on an internal "state", that changes with time and applied voltage. This causes the hysteresis in the IV curve.

Independent of the physical origin of these *states* it is now clear that they change slowly and differ with voltage. During the acquisition of a classical *IV curve* the cell changes from *state* to *state*, giving rise to the *IV curve* hysteresis. The *IV curve* hysteresis is therefore not a hysteresis in the classical sense originating from a material property in steady-state, but rather a measurement artifact occurring in non-steady-state characterization. It has been shown that the hysteresis is small at either very fast or very slow *IV ramps* [31, 46]. This is

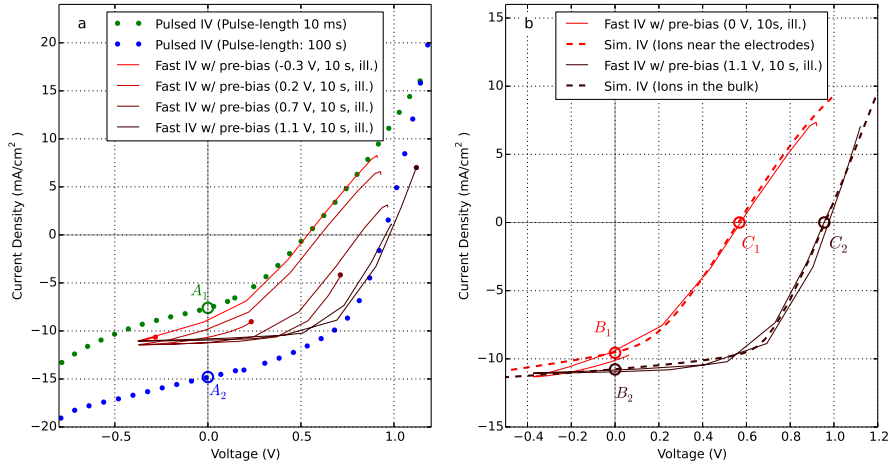


Figure 27: a) Measured IV curves with 10 millisecond and 100 second voltage and light pulses (points). The solid lines represent ramped IV measurements (70 V/s) with pre-bias under illumination for 10 seconds. States A_1 and A_2 are marked also in Figure 25a for clarity. b) Numerical drift-diffusion simulations of the IV curves with different ion distribution in comparison with the measured IV curves with pre-bias (same curves as in a). The simulation with ions close to the electrodes reproduces the measured IV curve with pre-bias at 0 Volt under illumination. Simulation with distributed ions reproduces the measured IV curve with pre-bias at 1.1 Volt and illumination. The states B_1 , B_2 , C_1 and C_2 are explained in detail in Figure 28.

explained if the ramp-rate is either significantly faster or slower than the time constant of these changing states.

Tress et al. [46] postulated mobile ions inside the perovskite layer being responsible for the internal state. Indeed Eames et al. [47] and Haruyama et al. [48] showed with density functional theory (DFT) calculations that iodide vacancies can move through the perovskite layer with an activation energy of 0.45 eV to 0.6 eV.

Tress et al. used a voltage pre-bias to condition the device followed by a fast IV ramp. Since the ramp-time is faster than the time-constant of the ionic movement, the full IV curve is acquired without affecting the distribution of the ions. Using a pre-bias voltage allows to change the position of the ions prior to the measurement. During fast acquisition of the IV curve the ion distribution can be considered to be “frozen” due to the small ion mobility. This is in contrast to the pulsed IV where for each voltage step the ions have time to migrate.

Fast IV curve measurements with 10 seconds voltage and light pre-bias are shown in solid lines in Figure 27a. The IV curve with -0.3 Volt pre-bias is close to the pulsed IV with 10 milliseconds duration. In both cases ions are close to their equilibrium distribution in the dark. Keeping the device even longer under illumination increases the current further to state A_2 . This indicates that light has also a direct or

Mobile ions inside the perovskite material may be responsible for the internal “state”.

IV curves are measured with a fast ramp after keeping the cell at a pre-bias voltage. Hereby ions are first positioned. The following IV curve is fast enough not to influence the position of the ions.

indirect influence on the ion position. An indirect influence could be the creation of charge carriers that change the electric field inside the device. The curves measured with different pre-bias voltage are shifted in voltage and have a different slope at forward current.

9.3.1 IV Curve Simulation

Physical processes are often too complex to understand with simple and qualitative explanations. Numerical simulations provide more insight and enable a broader understanding of underlying physics by putting hypotheses under test. Steady-state simulations of PSCs have recently been reported by Nie and co-workers [26]. Sun et al. [72] presented an elaborate analytical model to describe PSC IV curves.

The IV curves of the perovskite solar cell are simulated assuming ions at the interface or in the bulk.

To test the feasibility of the explanation with mobile ions we use numerical drift-diffusion to simulate IV curves with different ion distributions. Two states are simulated, one state with ions near the electrodes and one state with ions distributed homogeneously in the bulk. The ion distribution used in the simulation is displayed in Figure 28a (near the electrodes) and in Figure 28d (distributed in the bulk). The total number of ions is identical in both cases. The ions are modelled by two interface layers of 5 nanometer thickness that are doped. Drift and diffusion of electrons and holes is calculated, using bulk- and surface recombination. More details about the model are presented in the Section SIMULATION MODEL.

The IV curve simulations with different ion position reproduce the measured curves using different pre-bias voltages.

Figure 27b shows two measured IV curves (solid lines) once with pre-bias at 1.1 Volt and light, once with 0 Volt and light. Four points are marked (B_1 , B_2 , C_1 , C_2), which will be explained in Figure 28. The simulated IV curves are fitted to the fast IV curves with pre-bias voltage. The simulation is in good agreement with the measurement data as shown in Figure 27b. All parameters for the two IV curves are identical, except for the ion distribution, according to Figure 28a and Figure 28d. The simulation results show that the ions near the electrodes reduce the effective built-in field and therefore reduce the open-circuit voltage from C_2 to C_1 . The open-circuit voltage is reduced by 40% while the short-circuit current is reduced by 10%.

Both IV curves are simulated with the same parameters except the ion distribution.

Simulation parameters for both states are summarized in Table 2. The hole barrier at ETL is the difference between the HOMO level of perovskite and the TiO_2 (ETL). It is used to control the surface recombination at this contact. The same is the case for electrons at the spiro-OMeTAD (HTL). A negative energy barrier as used in this table indicates a high surface recombination.

Figure 28b shows the simulated energy bands at short-circuit (state B_1 of Figure 27b) with ions near the electrodes. Figure 28c shows bands for the same ion distribution at open-circuit (State C_1 of Figure 27b). Figure 28e and Figure 28f show short-circuit and open-circuit (state B_2 and C_2 of Figure 27b) with ions distributed in the

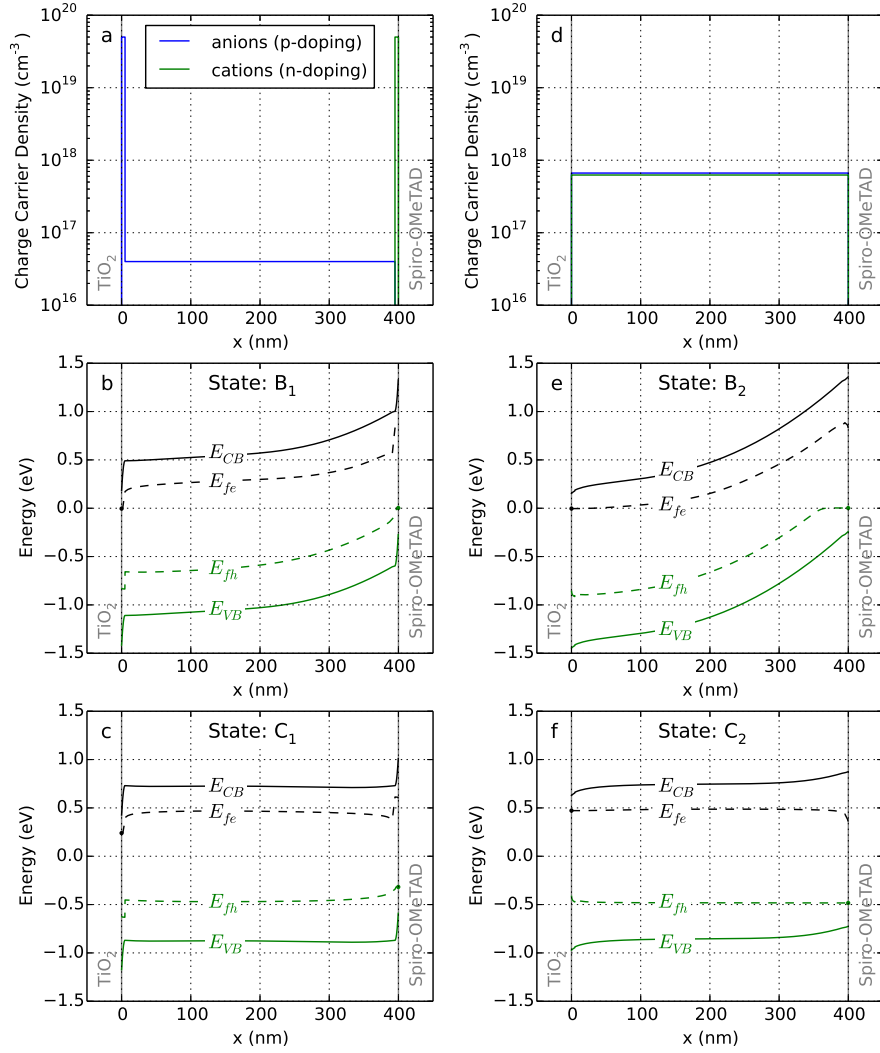


Figure 28: a) Assumed ion distribution inside the perovskite layer used for state B_1 and C_1 . Anions (-) near the TiO_2 layer and cations (+) near the spiroOMeTAD layer decrease the effective built-in field. Energy bands (E_{CB} and E_{VB}) and Fermi levels (E_{fe} , E_{fh}) with ion distribution of (a) at short-circuit under illumination, state B_1 (b) and at open-circuit, state C_1 (c), respectively. (d) Assumed ion distribution to simulate state B_2 and C_2 as shown in (e) and (f). States B_1 , B_2 , C_1 , C_2 are marked in Figure 27b.

Parameter	Value
Hole mobility μ_h	$0.15 \text{ cm}^2 / \text{Vs}$
Electron mobility μ_e	$2.4 \cdot 10^{-4} \text{ cm}^2 / \text{Vs}$
Recombination coefficient B	$7.3 \cdot 10^{-8} \text{ m}^3 / \text{s}$
n-doping N_D	$4 \cdot 10^{16} \text{ cm}^{-3}$
Ion charge at ETL for states (B_1, C_1)	$2.5 \cdot 10^{13} \text{ cm}^{-2}$
Ion charge at HTL for states (B_1, C_1)	$2.5 \cdot 10^{13} \text{ cm}^{-2}$
Ion charge at ETL for states (B_2, C_2)	0
Ion charge at HTL for states (B_2, C_2)	0
Hole barrier at ETL	-0.18 eV
Electron barrier at HTL	-0.28 eV
Electron density at ETL n_{e0}	$2.3 \cdot 10^{18} \text{ cm}^{-3}$
Hole density at HTL n_{h0}	$8 \cdot 10^{16} \text{ cm}^{-3}$
Relative electrical permittivity ϵ_r	35
Bandgap E_{BG}	1.6 eV
Series resistance R_S	59.9Ω
Thickness d	400 nm

Table 2: Parameters used for simulation of IV curves in Figure 27 and Figure 28.

Ions at the interface reduce the effective built-in voltage leading to smaller Fermi level gradient.

The internal field leads to a drift of mobile ions to the interface, partially compensating the internal field.

Under illumination the ions diffuse from the interface back to the bulk.

bulk. The Fermi levels in state B_2 are steep throughout the whole layer whereas in state B_1 Fermi levels are flat near the TiO_2 interface.

Therefore charge extraction is less efficient and the current is lower. The spikes in the bands close to the electrodes are caused by the charge of the ions. The ions close to the electrodes (state C_1) decrease the selectivity of both contacts, thus leading to an enhanced surface recombination and significantly lower open-circuit voltage [73, 74].

The reduced built-in voltage can be explained as follows: A p-type material has mobile holes and negatively charged ionic cores. In a p-i-n structure the negative ions of the p-type in combination with the positive ions of the n-type lead to an electric field in the intrinsic region. This field is called built-in field. With TiO_2 (n-type) and Spiro-OMeTAD (p-type) transport layers perovskite solar cells exhibit a built-in field. At short-circuit in the dark this built-in field leads to a drift of mobile cations (+) to the perovskite-spiro-OMeTAD interface and anions (-) to the perovskite- TiO_2 interface. The mobile cations (+) in the perovskite hereby partially compensate the fixed negative charge in the Spiro-OMeTAD. Therefore in the dark at short-circuit the built-in field is reduced. Under illumination the photo-generated charge disturbs the electric field. In this state the ions can diffuse away from the interface to the bulk. Therefore the built-in field in-

creases over illumination time. We illustrate this effect schematically in Figure 29.

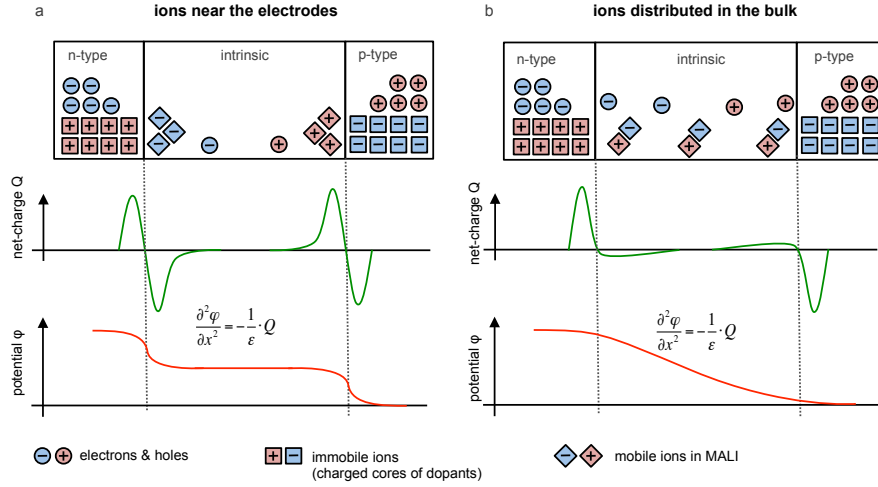


Figure 29: Schematic illustration of the effect of mobile ions on the potential. a) Ions are close to the interfaces and screen the electric field inside the bulk. The band is therefore flat. This is the state in the dark. b) Ions are distributed in the bulk and compensate each other. The potential drops over the whole intrinsic region leading to efficient charge extraction.

In contrast to Zhang et al. [33] that explained mobile ions schematically, the ions reduce the electric field in our case and the performance increases with time when ions relax. The difference lies in the cell architecture investigated. In our publication devices with selective contacts are used whereas Zhang et al. created a device with symmetric gold contacts. Zhang and co-workers used a bias voltage in forward direction to create an electric field and certain charge carrier selectivity. Therefore mobile ions enhance the performance and go to the opposite direction than in our case. The same effect is observed as switching PV [36, 37] and further confirms the mobile ion hypothesis.

With our proof-of-principle simulations we show that mobile ions are a plausible explanation for the observed **IV curve** hysteresis and the slow effects observed. According to these findings it seems best to track the maximum power point until stabilization in order to determine the power conversion efficiency of a perovskite solar cell.

In our case ions lead to a reduction of the built-in voltage, which is in contrast with other publications investigating mobile ions. The difference lies in the contacts.

Mobile ions are a plausible explanation for the hysteresis in perovskite solar cells.

9.4 FAST REGIME (MICROSECONDS TO MILLISECONDS)

In the previous section we have investigated the *slow* effects of the **TPC** measurement in Figure 25a. In this section the *fast* effects from 1 microsecond to 10 milliseconds are investigated. In this time regime mobile ions do not play a role, as they are too slow. We use the technique photo-generated charge extraction by linearly increasing

In the fast regime mobile ions can be considered as constant as they are too slow.

Charge carrier dynamics are investigated using the technique *photo-CELIV*.

The *CELIV*-current of the *PSC* shows two peaks indicating different electron and hole mobility.

Different values for the charge carrier mobility of perovskite have been published ranging from $20 \text{ cm}^2/\text{Vs}$ to $160 \text{ cm}^2/\text{Vs}$.

The cell investigated uses a TiO_2 scaffold. Electrons are most probably transported in the TiO_2 that has a mobility of around $10^{-2} \text{ cm}^2/\text{Vs}$. This difference in mobility could explain the two *CELIV*-peaks.

voltage (*photo-CELIV*) to analyse the charge carrier dynamics. *photo-CELIV* is a technique that is frequently used to measure the charge carrier mobility, recombination or doping in organic solar cells [63, 75–79]. In a previous publication we have shown that mobility extraction from *CELIV* data is error-prone [59, 80]. Nevertheless *CELIV* experiments give valuable insight into underlying physics of transport and recombination of photo-generated charges.

In the *photo-CELIV* experiment charge carriers are created by an LED pulse while the device is kept at open-circuit. Since the illumination time is short, a readjustment of the mobile ions is not expected. After turning off the light a voltage ramp in negative direction extracts all charge carriers. Usually one current peak is observed that is related with the faster charge carrier being extracted. The shorter the time of the current peak the higher the mobility of the charge carriers.

Figure 30a shows such *photo-CELIV* currents of the *PSC* with different voltage ramp rates A . The cell is illuminated for 1 millisecond and kept at open-circuit. At $t = 0$ the light is turned off and the voltage ramp $V(t) = V_{\text{OC}} - A \cdot t$ starts. For certain ramp rates two subsequent current peaks are observed. For the ramp rate ($A = 1.58 \text{ V/ms}$) a peak at about $4 \mu\text{s}$ appears followed by a second peak at $60 \mu\text{s}$. The second peak is visible in Figure 30b where the same data is plotted versus logarithmic time. In the measurement with the highest ramp rate ($A = 5 \text{ V/ms}$) only one current-peak is visible. The *photo-CELIV* results suggest that two charge carrier types are extracted causing the two current peaks. The amount of extracted charge varies significantly between the two carriers as indicated by the different peak height. Furthermore one carrier seems to be significantly faster than the other. From this we conclude a difference in the mobility.

Dong et al. [81] measured the charge carrier mobility in a perovskite single crystal by space-charge limited current (SCLC) on mono-polar devices using the Mott-Gurney Law. They found a mobility of $160 \text{ cm}^2/\text{Vs}$ for holes and $20 \text{ cm}^2/\text{Vs}$ for electrons. Leijtens et al. [65] however published balanced mobilities in planar devices of $20 \text{ cm}^2/\text{Vs}$ measured by photo-conductivity measurements. Balanced mobilities could also be expected from the similar effective mass of electron and holes [82]. Ponseca et al. [83] published time-resolved terahertz and microwave conductivity measurements and found balanced mobilities of $25 \text{ cm}^2/\text{Vs}$ in pure perovskite. They suggested however imbalanced mobilities in mesoporous scaffolds with TiO_2 . It is energetically favourable for electrons to transfer to TiO_2 . This process has been estimated to happen within picoseconds [84, 82, 51]. Electrons are in this case transported in the TiO_2 scaffold and not in perovskite. Since the mobility in TiO_2 has been published to be around $10^{-2} \text{ cm}^2/\text{Vs}$ [85] electrons are expected to be much slower in TiO_2 than in *MALI*. We therefore assume that the holes are the faster carriers creating the first peak in the *photo-CELIV* experiment

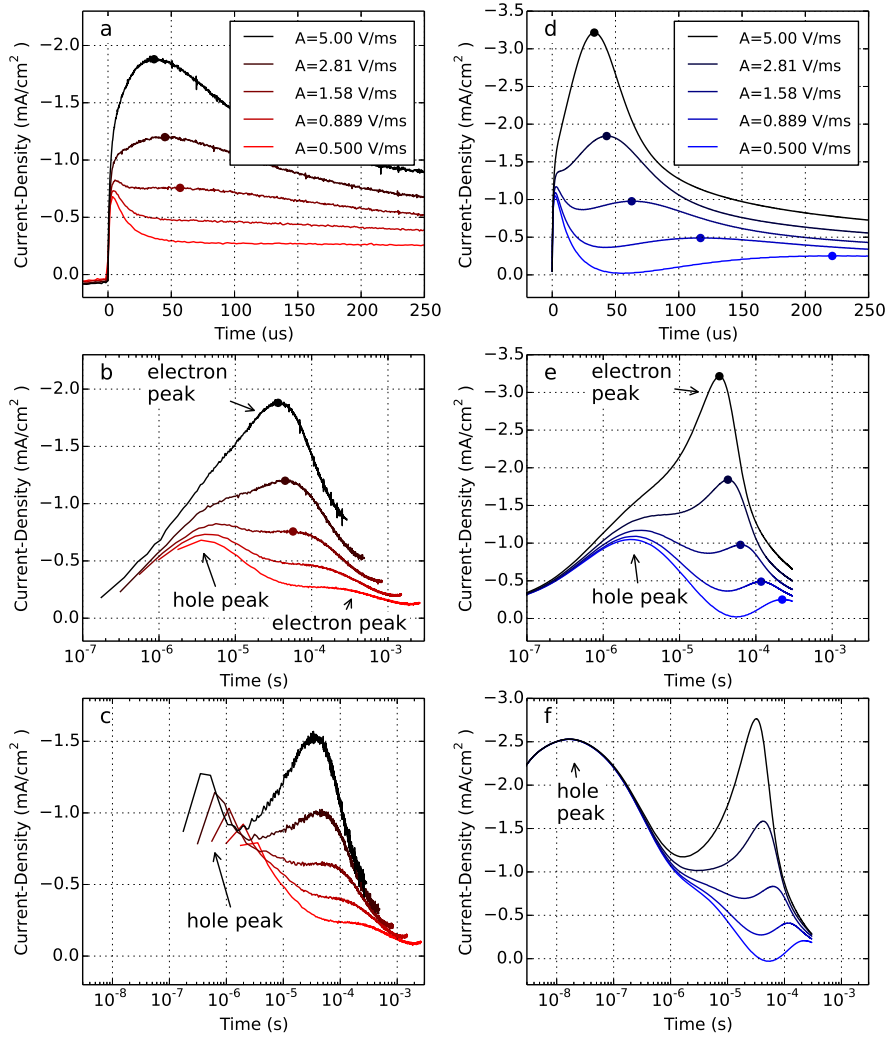


Figure 30: Measured **photo-CELIV** currents with 5 different ramp rates A in linear (a), in logarithmic time scale (b) and with correction of **RC effects** (c). The circle marks the second current peak. *Self-consistent* drift-diffusion simulations in (d), (e) and (f) respectively.

whereas the electrons cause the second peak. Electron and hole peaks are marked with arrows in **Figure 30**. An imbalance in mobility can also cause an imbalance in charge carrier density. The slower carrier is thereby limited by space charge effects and accumulates whereas the faster carrier leaves the device faster and accumulates on the electrodes outside of the bulk. This could in our case explain why more electrons than holes are extracted.

The question remains why there appears to be only one peak for the highest ramp rates ($A = 5 \text{ V/ms}$). In a previous publication we have shown that **RC effects** can significantly perturb **CELIV** measurements [59]. We therefore correct the **RC effects** by subtracting the displacement current of the measured current as proposed by Kettlitz and co-workers [86]. We assume that the device has a series resis-

RC effects can significantly perturb CELIV measurements.

tance caused by the sheet resistance of the TCO and the contact resistance that we summarize as R_S . The geometrical capacitance C_{geom} of the device is determined by the dielectric constants of the layers. We determine R_S to be 59.9Ω and C_{geom} to be 10.9 nF . Details on RC extraction can be found in Section [Determining series resistance and capacitance](#).

The CELIV current can be corrected for RC effects using a simple electric circuit.

We propose a simplified scheme of the solar cell to compensate RC effects as shown in [Figure 31](#). From i_{dev} (the measured current) and V_{dev} (the measured voltage) we calculate the corrected current i_{cell} according to [Equation 55](#). The derivation of [Equation 55](#) is found in Section [Derivation of the RC-Current Correction](#).

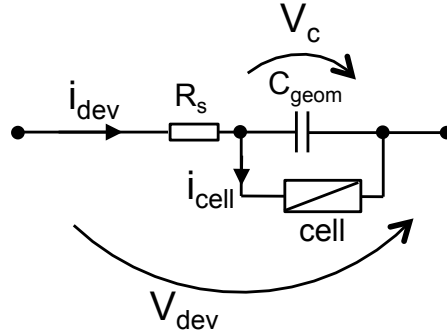


Figure 31: Electric circuit used to correct RC effects of CELIV measurements.

$$i_{cell}(t) = i_{dev}(t) - C_{geom} \cdot \frac{dV_{dev}}{dt} - R_S \cdot C_{geom} \cdot \frac{di_{dev}}{dt} \quad (55)$$

With the RC-correction the hole current peak shifts to the left (shorter times).

The RC correction is applied to the photo-CELIV data in [Figure 30a](#) and [Figure 30b](#). The RC corrected current is shown in [Figure 30c](#). Since the displacement current is corrected the total current is lower. Comparing the current with the lowest ramp rate ($A = 0.5 \text{ V/ms}$) in [Figure 30c](#) with [Figure 30b](#) it seems that the fast hole peak is amplified and at shorter time scales. RC effects have lowered and shifted the hole peak to longer times. With the RC correction this hole peak is recovered and visible in the currents of all ramp rates. The sub-microsecond hole peak is at the limit of the time resolution of our measurement, but can nevertheless be identified clearly. We show further below with numerical simulation that this peak shall not be taken as an artefact.

The holes are extracted first, as they have the higher mobility, leading to the first current peak. Electrons cause the second peak.

We conclude that before their extraction electrons and holes accumulate in the bulk. The amount of electrons in the bulk exceeds the amount of holes in the bulk. The rest of the holes has left the device and accumulates on the electrode. As the voltage ramp starts, holes move out of the device quickly. In the case of the high ramp rate ($A = 5 \text{ V/ms}$) holes are not detectable in the outer device current. The holes only charge the capacitance of the cell. We will strengthen

this hypothesis further below in the text when we discuss numerical simulations in [Figure 30d](#), [Figure 30e](#) and [Figure 30f](#).

We now discuss the origin of the imbalanced charge carrier density before the voltage ramp. Imbalanced charge in the device can be caused by an imbalance in charge carrier mobility (as mentioned above), asymmetric extraction barriers, charge doping or trapping. As shown above, there is evidence for imbalanced mobilities. The question therefore is, if other effects further enhance the imbalance. To further investigate the imbalance of charge carrier density, the illumination duration prior to the charge extraction by linearly increasing voltage (CELIV) voltage ramp is varied. [Figure 32a](#) shows RC-corrected [photo-CELIV](#) currents with varied illumination duration prior to the voltage ramp. In the case of short illumination duration ($t_{ill} = 100 \mu s$) the hole peak is high and the subsequent electron peak is low. With longer illumination time the hole peak decreases whereas the electron peak increases. This result suggests that the imbalance of charge carrier density is increasing with illumination duration. Assuming the mobility to be constant in time the mobility imbalance cannot be the origin of this increase.

Why are there much more electrons than holes extracted?

The charge imbalance increases with time as shown in the [photo-CELIV](#) measurement with varied illumination duration.

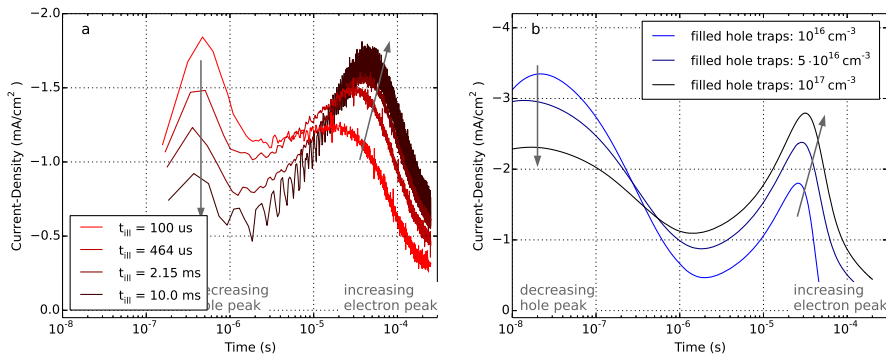


Figure 32: a) Measured [photo-CELIV](#) currents using constant ramp rate ($A = 5 mV/s$) and varied illumination duration prior to the ramp. b) Simulated [photo-CELIV](#) currents using different densities of filled traps. Curves in a) and b) are RC corrected with [Equation 55](#).

As commonly known charge doping leads to an imbalanced charge carrier density. In most solar cells, like crystalline silicon or [CIGS](#), this is the case. But classical doping is constant in time and would not lead to the effects observed in [Figure 32a](#). Captured charges in deep traps however behave like ionized dopants, too. Occupied traps have the same effect as the same amount of dopants. Leijtens and Stranks et al. [65, 68] have observed a doping effect of traps in perovskite cells. They also showed evidence for trap-assisted recombination. Baumann et al. [87] showed the presence of deep trap states, estimated at a depth of $0.5 eV$, with thermally stimulated current (TSC). The question about the nature of the traps was addressed in the literature.

With longer illumination duration holes get trapped leading to an increased ratio of free electrons to free holes.

Trapping can cause an imbalance in charge carrier density very similar to classical doping.

The more holes get trapped the higher the ratio of free electrons to free holes. With illumination duration the charge imbalance increases and more electrons are extracted.

Transient simulations are used to reproduce the measured photo-CELIV currents.

The simulated photo-CELIV currents reproduce the effects of the measurement qualitatively for the different ramp rates.

DFT simulations show that anion-cation substitutions (iodide replacing lead or MA) can act as deep hole traps [27, 49].

Our qualitative understanding is thus as follows: If a hole is trapped it is immobile like an ionized dopant and leads indirectly to an additional free electron. This may not be intuitive:

Imagine an empty semiconductor with deep hole traps. One photon is absorbed - a free electron and a free hole are created. After the hole has been trapped, there is a free electron left. There is no difference compared to an empty semiconductor with one electron dopant.

With longer illumination duration traps become more and more filled. Therefore the amount of free electrons increases. The amount of free holes decreases since they encounter more recombination partners. Therefore deep hole trapping is assumed to lead to an additional imbalance of charge carrier density. Further evidence for charge trapping is the long and steady current-decay in the voltage-pulse experiment shown in Figure 25b. Knapp et al. [88] presented numerical simulations of dark injection transients (DIT) (voltage pulses) with fast and slow traps leading to a similar current decay as observed in this thesis.

9.4.1 Photo-CELIV Simulations

Above photo-CELIV measurements with qualitative explanations were presented. To confirm these findings we perform numerical drift-diffusion simulations of the photo-CELIV experiments. Details on the simulation model can be found in section SIMULATION MODEL.

In this state the mobile ions are close to the electrodes (see Figure 28a). Therefore we use a small charge carrier density as boundary condition. For simplicity we use n-type doping to mimic filled hole traps. The series-resistance R_S is considered in the simulation because RC effects play an important role in the transient measurements [59, 86].

Figure 30d and Figure 30e show the simulation results of the CELIV-currents using the same experimental conditions as in the measurement. A good qualitative agreement is achieved for this variation of ramp rates and wide range of time scales. The simulation here is not meant to quantitatively extract material parameters but rather to derive an understanding of the operating mechanisms in a broad time range. The main dynamics are reproduced: For small ramp rates the hole current peak and the subsequent electron current peak are visible. For the largest ramp rate the hole peak vanishes and only the electron peak is observed. In the simulation we consider the series resistance R_S to cause RC effects and then apply the same

RC correction to the simulated data, like in the case of the measured data (see Figure 30f). Thus Figure 30c and Figure 30f can directly be compared. This consistency validates our approach of the RC correction. The initial peak is similar as in the measurement.

We use the same simulation parameters to explain the photo-CELIV experiment with varied illumination duration (see Figure 32b). Here the doping density is varied between 10^{16} 1/cm^3 and 10^{17} 1/cm^3 to control the amount of trapped holes. The effect of the imbalanced charge carrier density is reproduced. The first peak decreases as fewer holes are around and the second peak increases due to the accumulation of electrons in the bulk.

Table 3 summarizes the simulation parameters used for the simulation of the CELIV currents. The parameters used here are not identical as the one used for the IV curve simulations in Table 2. To optimize simulation convergence and speed the 5 nm layers containing the ionic charge (ions at the interface) were omitted and the charge densities at the interface (n_{e0} and n_{h0}) were reduced to 10^{12} cm^{-3} . This results in a similar built-in voltage as in the case with the ion layers. The charge carrier mobilities used in the transient simulations are significantly higher compared to the IV curve simulations. Also the surface recombination is very low compared to Table 2.

Parameter	Value
Hole mobility μ_h	$1 \text{ cm}^2/\text{Vs}$
Electron mobility μ_e	$0.2 \text{ cm}^2/\text{Vs}$
Recombination coefficient B	$5.2 \cdot 10^{-9} \text{ m}^3/\text{s}$
n-doping N_D (varied in Figure 32)	$1 \cdot 10^{16}$ to $1 \cdot 10^{17} \text{ cm}^{-3}$
Hole barrier at ETL	0.3 eV
Electron barrier at HTL	0.3 eV
Electron density at ETL n_{e0}	$1 \cdot 10^{12} \text{ cm}^{-3}$
Hole density at HTL n_{h0}	$1 \cdot 10^{12} \text{ cm}^{-3}$
Relative electrical permittivity ϵ_r	35
Bandgap E_{BG}	1.6 eV
Series resistance R_S	59.9Ω
Thickness d	400 nm

Table 3: Parameters used for simulation of the photo-CELIV experiments in Figure 30 and Figure 32.

The hypothesis with imbalanced mobilities and deep trapping seems to be a plausible explanation for the photo-CELIV currents presented in this thesis.

The simulation also reproduces the CELIV with varied illumination duration.

The simulation parameters for the IV curve simulation and the CELIV simulation are not identical. The simulations shall be seen as "proof-of-principle", showing the plausibility of the explanation of the physical effects discussed in this thesis.

9.5 LIMITATION OF THE APPROACH

The presented model is used for qualitative understanding, not for parameter extraction.

A fully consistent model has not been shown in the literature so far. The presented work shows that the current model is nevertheless able to describe the effects in the measurements.

We would like to emphasize that we do not present a fully consistent model for transient and steady-state characterization as we published for an organic solar cell in Ref [60]. The model parameter set for the [IV curves](#) and for the [CELIV](#) currents is not identical. The focus of the model is on qualitative agreement and understanding. The dynamics of ionic motion is not modelled. The dynamics of trapping and detrapping are not modelled. Therefore the curves in [Figure 25a](#) and [Figure 25b](#) going from microsecond to minutes cannot yet be reproduced with one model. Future model refinements will address these issues. The presented work illustrates that the currently limited model is nevertheless able to describe the effects in the measurements.

DISCUSSION

In summary we postulate imbalanced mobilities in combination with traps to be responsible for the space charge effects on short time scales and mobile ions for the change of field distribution on longer time scales. With our numerical model we show that this explanation is plausible and the measurement results can be reproduced. In this section we discuss additional physical effects that could play a role.

10.1 TIME DEPENDENT CHARGE GENERATION

Analysing the current rise in [Figure 25a](#) one could speculate on time-dependent charge carrier generation. If [exciton](#) dissociation was dependent on the electric field this could be the case. There is an ongoing scientific debate about the [exciton](#) binding energy in [MALI](#) perovskite. Theoretical calculations by Frost et al. [89] predict 0.7 meV . Different measurements were published: 37 meV by Hirasawa et al. [90] already in 1994, 19 meV at low temperature by Sun et al. [91], 16 meV at low temperature by Miyata and co-workers [92]. [Exciton](#) dissociation is expected to take place even without an electric field at room temperature ($kT = 26\text{ meV}$). Furthermore O'Regan et al. [71] suggest no change in separation efficiency based on calculations of recombination fluxes. Deschler et al. [52] showed free charge carrier generation after 1 ps . We therefore consider direct charge generation from photons and neglect the intermediate [exciton](#) state in our model.

Time dependent charge generation is improbable because the [exciton](#) binding energy is very low.

10.2 DIPOLES, INTERFACE-TRAPS AND FERROELECTRICITY

Our results suggest a slow change in the electric field caused by a change of interfacial charge. Ferroelectricity is expected to change the width of the space-charge region [43] due to a change in electrical permittivity. But changing the relative electric permittivity in the model has only very little influence on the shape of the [IV curve](#). By rotation of dipoles in large ferroelectric domains however the same effect of a change in surface charge would be observed. With our model we can therefore not exclude ferroelectricity to play a role. Electron traps at the TiO_2 interface could also lead to the same change in charge close to the interface. Questionable here is why trapped electrons at the TiO_2 interface would depopulate under illumination. By looking at the dynamics of [Figure 25a](#), mobile ions seem the most plausible explanation. Interface trapping and ferroelectricity can however not be fully excluded.

Instead of mobile ions also dipoles or interface traps could cause the change in built-in voltage. With our approach this cannot be excluded.

10.3 EXCLUDING SPECIFIC FABRICATION ISSUES

Different device architectures were measured to exclude issues in fabrication.

In order to exclude the possibility that specific issues in the device fabrication cause these effects we have measured PSCs from three different groups and with different structures (TiO_2 scaffold, Al_2O_3 scaffold, planar). All cells show a current rise with a dynamic range over at least 6 orders of magnitude in time – Similar as in Figure 25. We conclude that traps and mobile ions are present in all these structures although the charge carrier dynamics varies between the device types. We measured 9 devices in total but show here only results of one device for consistency and simplicity.

10.4 OPEN QUESTIONS

*How do the bulk properties change when ions move?
Why does the hysteresis depend on the contact material?
What is the effect of surface passivation on the hysteresis?*

An open question remains on how ion migration affects the bulk properties. Is the trap and doping density inside the device dependent on the position of the mobile ions? Or to put it differently: How is the bulk material quality affected when interstitials or vacancies move to the electrodes due to an electric field? It has been shown that devices with P3HT and PCBM as contact material show much less IV curve hysteresis [26, 33]. If the IV curve hysteresis is caused by ion migration, why does it depend on the contact material? One could speculate that ion migration takes place independent of the contact material, but is more detrimental to cell performance if the surface recombination is high. With passivated surfaces the reduced built-in field might be irrelevant since the charge carriers can diffuse out of the device in any case – with or without an electric field.

Part V

SUMMARY AND OUTLOOK

SUMMARY

Voltage pulse and light pulse measurements of methylammonium lead iodide (MALI) perovskite solar cells are presented with a time range spanning 9 orders of magnitude. A “fast regime” from microseconds to milliseconds and a “slow regime” from milliseconds to minutes are identified.

Pulsed IV curves measured with different pulse-lengths and fast ramped IV curves with voltage pre-bias explain the “slow regime”. Drift-diffusion simulations with different ion positions explain the experimental results and strengthen the hypothesis of mobile ions as explanation for the IV curve hysteresis in perovskite solar cells. photo-CELIV experiments with different ramp rates and different illumination times are used to shed light on and explain the “fast regime”. Transient drift-diffusion calculation is applied to understand the observed experimental results. The hypothesis of imbalanced charge carrier mobilities and deep hole traps is very plausible as the model-based analysis shows.

In a next step the numerical model could be extended with ion migration enabling the simulation of the full transient experiments. With this approach we are on the way to a complete model describing charge transport in perovskite solar cells from microseconds to minutes after excitation.

OUTLOOK

The development of perovskite solar cells is still at the beginning. In order to become commercially relevant the device stability needs to be improved. Dye Sol recently presented a perovskite solar cell being stable over 1000 hours [93]. Silicon solar module manufacturers offer a warranty over 20 years which corresponds to more than 20'000 hours of operation. Reaching comparable device stability will be one of the major challenges for perovskite devices.

The toxicity needs to be investigated in more detail and environmental compatibility of modules needs to be proven. Perovskite containing lead or tin will probably not play a role in consumer electronics due to its toxicity.

There are two main applications where perovskites could play a role in the future. Either in cheap perovskite modules or in **tandem** configurations with conventional solar cells.

The current PV market is dominated by silicon wafer-based modules. As silicon solar cells are approaching their maximum theoretical efficiency the room for improvements with the current technology gets smaller. Using a **tandem** configuration with a perovskite top cell and a silicon bottom cell could reach efficiencies up to 30% [94].

So far 4-terminal **tandems** with perovskite top cell and crystalline silicon bottom cell reaching 17% have been demonstrated [95]. By using perovskite on top of a **CIGS** cell in 4-terminal configuration 19.5% **PCE** were reached [96]. In perovskite-silicon 2-terminal cell configuration 18.1% were demonstrated [97]. These results are promising as they could be easily added in a silicon solar cell production line.

Whatever application will become relevant for perovskite devices, further insight into the physical device operating mechanism will be essential to improve efficiency and lifetime. New measurement techniques like the transient photocurrent (**TPC**) presented in this paper can help to understand physical effects. To characterize devices with mobile ions, very systematic data acquisition is a necessity and all experiments need to be done with preconditioning. Yet, there is no physical model that describes the physics of a perovskite solar cell completely. Models incorporating mobile ions in a drift-diffusion calculation will be a step in that direction.

To improve absorption light trapping structures suitable for perovskite need to be developed and optimized by numerical simulation. Fluxim has developed a prototype solver to calculate light scattering properties combining ray-tracing and thin-film optics leading towards comprehensive opto-electronic simulation of silicon-perovskite

The major challenge for perovskite solar cells will be the device stability. So far 1000 hours of operation have been demonstrated.

*With silicon perovskite **tandems** efficiencies of 30% could be realized.*

Further insight into device physics will be necessary to improve efficiency and lifetime. To characterise devices with mobile ions very systematic experiments are required.

[tandems](#). On the long run module modelling can help optimising the grid and module structure.

Much research effort will be required that perovskite once generates electricity on our rooftops.

ACKNOWLEDGEMENT

I would like to acknowledge the following individuals that supported this work in one or the other way.

- Beat Ruhstaller (Fluxim AG, ZHAW) for supervising
- Uli Würfel, Birger Zimmermann (Fraunhofer ISE), Stephane Al-tazin, Lieven Penninck (Fluxim AG) and Oskar Sandberg (Abo Akademi University) for fruitful discussions
- Simon Züfle (ZHAW) for proof-reading and discussions
- Adrian Gentsch (Fluxim AG) for collaboration on the *Paicos* development
- Kurt Pernstich (ZHAW) for providing access to the glove-box at ZHAW
- Philipp Löper, Jeremie Werner, Bjoern Niesen and Christophe Ballif (EPFL IMT) for the fabrication of the perovskite solar cells and for discussions
- Cyrill Bolliger for providing the LaTeX template

Part VI

APPENDIX

APPENDIX

14.1 ABBREVIATIONS

CdTe	cadmium telluride
CIGS	copper indium gallium diselenide
MOCVD	metal organic chemical vapor deposition
DSSC	dye sensitized solar cell
OSC	organic solar cell
PCE	power conversion efficiency
MALI	methyammonium lead iodide
PSC	perovskite solar cell
TEL	transient electroluminescence
TPV	transient photo-voltage
CELIV	charge extraction by linearly increasing voltage
photo-CELIV	photo-generated charge extraction by linearly increasing voltage
TPC	transient photocurrent
SCLC	space-charge limited current
SRH	Shockley-Read-Hall
NREL	National Renewable Energy Laboratory
HOMO	highest occupied molecular orbit
LUMO	lowest unoccupied molecular orbit
DFT	density functional theory
TCO	transparent conducting oxide
ETL	electron transport layer
HTL	hole transport layer
IV curve	Current-voltage curve

TSC	thermally stimulated current
DIT	dark injection transients
EQE	external quantum efficiency
MPP	maximum power point
EL	electroluminescence
IPCC	Intergovernmental Panel Climate Change
RCP	representative concentration pathway

BIBLIOGRAPHY

-
- [1] Thomas F. Stocker. Climate change 2013: The physical science basis, fifth assessment report. URL <http://www.ipcc.ch/>. (Cited on pages 9 and 10.)
 - [2] Global Market Outlook 2015-2019, . (Cited on pages 11 and 12.)
 - [3] Global Wind Statistics 2012. (Cited on page 12.)
 - [4] Key World Energy Statistics 2014. (Cited on page 12.)
 - [5] Current and Future: Cost of Photovoltaics. (Cited on page 13.)
 - [6] Photovoltaics Report, Fraunhofer-Institut für Solare Energiesysteme ISE. (Cited on pages 13 and 17.)
 - [7] Harry Wirth. Fakten zur PV. (Cited on pages 13 and 14.)
 - [8] Niklaus Zepf. Stromperspektiven 2020, Neue Erkenntnisse, Axpo Holding AG. (Cited on pages 13 and 14.)
 - [9] Stickelberger. SwissSolar. (Cited on page 14.)
 - [10] Martin A. Green, Keith Emery, Yoshihiro Hishikawa, Wilhelm Warta, and Ewan D. Dunlop. Solar cell efficiency tables (version 46): Solar cell efficiency tables (version 46). 23(7):805–812. ISSN 10627995. URL <http://doi.wiley.com/10.1002/pip.2637>. (Cited on pages 16 and 17.)
 - [11] Solarte, Belectric, www.solarte.de, . URL www.solarte.de. (Cited on page 16.)
 - [12] Jeong-Hyeok Im, Chang-Ryul Lee, Jin-Wook Lee, Sang-Won Park, and Nam-Gyu Park. 6.5% efficient perovskite quantum-dot-sensitized solar cell. 3(10):4088, . ISSN 2040-3364, 2040-3372. URL <http://xlink.rsc.org/?DOI=c1nr10867k>. (Cited on page 16.)
 - [13] Mark Gruber, Julia Wagner, Konrad Klein, Ulrich Hörmann, Andreas Opitz, Martin Stutzmann, and Wolfgang Brütting. Thermodynamic Efficiency Limit of Molecular Donor-Acceptor Solar Cells and its Application to Diindenoperylene/C60-Based Planar Heterojunction Devices. 2(9):1100–1108. ISSN 16146832. URL <http://doi.wiley.com/10.1002/aenm.201200077>. (Cited on page 17.)

- [14] Research Cell Efficiency Records, National Renewable Energy Laboratory (NREL), http://www.nrel.gov/ncpv/images/efficiency_chart.jpg, 5.10.2016. URL http://www.nrel.gov/ncpv/images/efficiency_chart.jpg. (Cited on pages 17 and 18.)
- [15] A. Virtuani, D. Pavanello, and G. Friesen. Overview of temperature coefficients of different thin film photovoltaic technologies. In *25th European Photovoltaic Solar Energy Conference and Exhibition/5th World Conference on Photovoltaic Energy Conversion*, pages 6–10. (Cited on page 17.)
- [16] E. A. Katz, D. Faiman, S. M. Tuladhar, J. M. Kroon, M. M. Wienk, T. Fromherz, F. Padinger, C. J. Brabec, and N. S. Sariciftci. Temperature dependence for the photovoltaic device parameters of polymer-fullerene solar cells under operating conditions. 90 (10):5343. ISSN 00218979. URL <http://scitation.aip.org/content/aip/journal/jap/90/10/10.1063/1.1412270>. (Cited on page 17.)
- [17] Moritz Riede, Christian Uhrich, Johannes Widmer, Ronny Timmreck, David Wynands, Gregor Schwartz, Wolf-Michael Gnehr, Dirk Hildebrandt, Andre Weiss, Jaehyung Hwang, Sudhakar Sundarraj, Peter Erk, Martin Pfeiffer, and Karl Leo. Efficient Organic Tandem Solar Cells based on Small Molecules. 21(16):3019–3028. ISSN 1616301X. URL <http://doi.wiley.com/10.1002/adfm.201002760>. (Cited on page 17.)
- [18] Hyun Suk Jung and Nam-Gyu Park. Perovskite Solar Cells: From Materials to Devices. 11(1):10–25. ISSN 16136810. URL <http://doi.wiley.com/10.1002/sml.201402767>. (Cited on pages 17, 19 and 20.)
- [19] Dirk C. Jordan and Sarah R. Kurtz. Photovoltaic degradation rates—an analytical review. 21(1):12–29. URL <http://onlinelibrary.wiley.com/doi/10.1002/pip.1182/full>. (Cited on pages 17 and 18.)
- [20] Nam-Gyu Park. Perovskite solar cells: An emerging photovoltaic technology. 18(2):65–72, . ISSN 13697021. URL <http://linkinghub.elsevier.com/retrieve/pii/S1369702114002570>. (Cited on page 18.)
- [21] Akihiro Kojima, Kenjiro Teshima, Yasuo Shirai, and Tsutomu Miyasaka. Organometal Halide Perovskites as Visible-Light Sensitizers for Photovoltaic Cells. 131(17):6050–6051. ISSN 0002-7863, 1520-5126. URL <http://pubs.acs.org/doi/abs/10.1021/ja809598r>. (Cited on page 19.)

- [22] Hui-Seon Kim, Chang-Ryul Lee, Jeong-Hyeok Im, Ki-Beom Lee, Thomas Moehl, Arianna Marchioro, Soo-Jin Moon, Robin Humphry-Baker, Jun-Ho Yum, Jacques E. Moser, Michael Grätzel, and Nam-Gyu Park. Lead Iodide Perovskite Sensitized All-Solid-State Submicron Thin Film Mesoscopic Solar Cell with Efficiency Exceeding 9%. 2, . ISSN 2045-2322. URL <http://www.nature.com/doifinder/10.1038/srep00591>. (Cited on page 19.)
- [23] Xiaoxi He. Perovskite photovoltaics: Current status and outlook. 2(3):030301. ISSN 2053-1613. URL <http://stacks.iop.org/2053-1613/2/i=3/a=030301?key=crossref.a11d0e6e9169275a6bf8b827e19570c4>. (Cited on page 19.)
- [24] Byung-Wook Park, Bertrand Philippe, Xiaoliang Zhang, Håkan Rensmo, Gerrit Boschloo, and Erik M. J. Johansson. Bismuth Based Hybrid Perovskites $A_3Bi_2I_9$ (A: Methylammonium or Cesium) for Solar Cell Application. pages n/a–n/a. ISSN 09359648. URL <http://doi.wiley.com/10.1002/adma.201501978>. (Cited on page 19.)
- [25] Peng Gao, Michael Grätzel, and Mohammad K. Nazeeruddin. Organohalide lead perovskites for photovoltaic applications. 7 (8):2448. ISSN 1754-5692, 1754-5706. URL <http://xlink.rsc.org/?DOI=C4EE00942H>. (Cited on page 19.)
- [26] W. Nie, H. Tsai, R. Asadpour, J.-C. Blancon, A. J. Neukirch, G. Gupta, J. J. Crochet, M. Chhowalla, S. Tretiak, M. A. Alam, H.-L. Wang, and A. D. Mohite. High-efficiency solution-processed perovskite solar cells with millimeter-scale grains. 347(6221):522–525. ISSN 0036-8075, 1095-9203. URL <http://www.sciencemag.org/cgi/doi/10.1126/science.aaa0472>. (Cited on pages 20, 64 and 76.)
- [27] Wan-Jian Yin, Tingting Shi, and Yanfa Yan. Unusual defect physics in $CH_3NH_3PbI_3$ perovskite solar cell absorber. 104(6): 063903, . ISSN 0003-6951, 1077-3118. URL <http://scitation.aip.org/content/aip/journal/apl/104/6/10.1063/1.4864778>. (Cited on pages 20 and 72.)
- [28] M. M. Lee, J. Teuscher, T. Miyasaka, T. N. Murakami, and H. J. Snaith. Efficient Hybrid Solar Cells Based on Meso-Superstructured Organometal Halide Perovskites. 338(6107): 643–647. ISSN 0036-8075, 1095-9203. URL <http://www.sciencemag.org/cgi/doi/10.1126/science.1228604>. (Cited on page 20.)
- [29] Mingzhen Liu, Michael B. Johnston, and Henry J. Snaith. Efficient planar heterojunction perovskite solar cells by vapour

- deposition. 501(7467):395–398, . ISSN 0028-0836, 1476-4687. URL <http://www.nature.com/doi/abs/10.1038/nature12509>. (Cited on page 20.)
- [30] Henry J. Snaith, Antonio Abate, James M. Ball, Giles E. Eperon, Tomas Leijtens, Nakita K. Noel, Samuel D. Stranks, Jacob Tse-Wei Wang, Konrad Wojciechowski, and Wei Zhang. Anomalous Hysteresis in Perovskite Solar Cells. 5(9):1511–1515. ISSN 1948-7185. URL <http://pubs.acs.org/doi/abs/10.1021/jz500113x>. (Cited on pages 20, 21 and 59.)
- [31] E. L. Unger, E. T. Hoke, C. D. Bailie, W. H. Nguyen, A. R. Bowring, T. Heumüller, M. G. Christoforo, and M. D. McGehee. Hysteresis and transient behavior in current–voltage measurements of hybrid-perovskite absorber solar cells. 7(11):3690–3698. ISSN 1754-5692, 1754-5706. URL <http://xlink.rsc.org/?DOI=C4EE02465F>. (Cited on pages 20, 21, 59 and 62.)
- [32] Ronen Gottesman, Eynav Haltzi, Laxman Gouda, Shay Tirosh, Yaniv Bouhadana, Arie Zaban, Edoardo Mosconi, and Filippo De Angelis. Extremely Slow Photoconductivity Response of $\text{CH}_3\text{NH}_3\text{PbI}_3$ Perovskites Suggesting Structural Changes under Working Conditions. 5(15):2662–2669. ISSN 1948-7185. URL <http://pubs.acs.org/doi/abs/10.1021/jz501373f>. (Cited on pages 21 and 60.)
- [33] Ye Zhang, Mingzhen Liu, Giles E. Eperon, Tomas C. Leijtens, David McMeekin, Michael Saliba, Wei Zhang, Michele de Bastiani, Annamaria Petrozza, Laura M. Herz, Michael B. Johnston, Hong Lin, and Henry J. Snaith. Charge selective contacts, mobile ions and anomalous hysteresis in organic–inorganic perovskite solar cells. 2(3):315–322. ISSN 2051-6347, 2051-6355. URL <http://xlink.rsc.org/?DOI=C4MH00238E>. (Cited on pages 21, 67 and 76.)
- [34] Bo Wu, Kunwu Fu, Natalia Yantara, Guichuan Xing, Shuangyong Sun, Tze Chien Sum, and Nripan Mathews. Charge Accumulation and Hysteresis in Perovskite-Based Solar Cells: An Electro-Optical Analysis. pages n/a–n/a. ISSN 16146832. URL <http://doi.wiley.com/10.1002/aenm.201500829>. (Cited on page 20.)
- [35] Emilio J. Juarez-Perez, Rafael S. Sanchez, Laura Badia, Germá Garcia-Belmonte, Yong Soo Kang, Ivan Mora-Sero, and Juan Bisquert. Photoinduced Giant Dielectric Constant in Lead Halide Perovskite Solar Cells. 5(13):2390–2394. ISSN 1948-7185. URL <http://pubs.acs.org/doi/abs/10.1021/jz5011169>. (Cited on page 20.)

- [36] Nam-Gyu Park. Perovskite solar cells: Switchable photovoltaics. . URL <http://www.nature.com/nmat/journal/vaop/ncurrent/full/nmat4177.html>. (Cited on pages 20 and 67.)
- [37] Zhengguo Xiao, Yongbo Yuan, Yuchuan Shao, Qi Wang, Qingfeng Dong, Cheng Bi, Pankaj Sharma, Alexei Gruverman, and Jinsong Huang. Giant switchable photovoltaic effect in organometal trihalide perovskite devices. 14(2):193–198. ISSN 1476-1122, 1476-4660. URL <http://www.nature.com/doifinder/10.1038/nmat4150>. (Cited on pages 20, 21 and 67.)
- [38] Ajay Kumar Jena, Hsin-Wei Chen, Atsushi Kogo, Yoshitaka Sane-hira, Masashi Ikegami, and Tsutomu Miyasaka. The Interface between FTO and the TiO_2 Compact Layer Can Be One of the Origins to Hysteresis in Planar Heterojunction Perovskite Solar Cells. 7(18):9817–9823. ISSN 1944-8244, 1944-8252. URL <http://pubs.acs.org/doi/abs/10.1021/acsami.5b01789>. (Cited on page 21.)
- [39] Bo Chen, Xiaojia Zheng, Mengjin Yang, Yuan Zhou, Souvik Kundu, Jian Shi, Kai Zhu, and Shashank Priya. Interface band structure engineering by ferroelectric polarization in perovskite solar cells. 13:582–591, . ISSN 22112855. URL <http://linkinghub.elsevier.com/retrieve/pii/S221128551500141X>. (Cited on page 21.)
- [40] Chong Liu, Jiandong Fan, Xing Zhang, Yanjiao Shen, Lin Yang, and Yaohua Mai. Hysteretic Behavior upon Light Soaking in Perovskite Solar Cells Prepared via Modified Vapor-Assisted Solution Process. 7(17):9066–9071, . ISSN 1944-8244, 1944-8252. URL <http://pubs.acs.org/doi/abs/10.1021/acsami.5b00375>.
- [41] Hui-Seon Kim, Sung Kyun Kim, Byeong Jo Kim, Kyung-Sik Shin, Manoj Kumar Gupta, Hyun Suk Jung, Sang-Woo Kim, and Nam-Gyu Park. Ferroelectric Polarization in $\text{CH}_3\text{NH}_3\text{PbI}_3$ Perovskite. 6(9):1729–1735, . ISSN 1948-7185. URL <http://pubs.acs.org/doi/abs/10.1021/acs.jpcclett.5b00695>.
- [42] Jarvist M. Frost, Keith T. Butler, and Aron Walsh. Molecular ferroelectric contributions to anomalous hysteresis in hybrid perovskite solar cells. 2(8):081506, . ISSN 2166-532X. URL <http://scitation.aip.org/content/aip/journal/aplmater/2/8/10.1063/1.4890246>.
- [43] Jing Wei, Yicheng Zhao, Heng Li, Guobao Li, Jinlong Pan, Dongsheng Xu, Qing Zhao, and Dapeng Yu. Hysteresis Analysis Based on the Ferroelectric Effect in Hybrid Perovskite Solar Cells. 5(21):3937–3945. ISSN 1948-7185. URL <http://pubs.acs.org/doi/abs/10.1021/jz502111u>. (Cited on page 75.)

- [44] Hsin-Wei Chen, Nobuya Sakai, Masashi Ikegami, and Tsutomu Miyasaka. Emergence of Hysteresis and Transient Ferroelectric Response in Organo-Lead Halide Perovskite Solar Cells. 6(1): 164–169, . ISSN 1948-7185. URL <http://pubs.acs.org/doi/abs/10.1021/jz502429u>. (Cited on page 21.)
- [45] Fan Zheng, Hiroyuki Takenaka, Fenggong Wang, Nathan Z. Koocher, and Andrew M. Rappe. First-Principles Calculation of the Bulk Photovoltaic Effect in $\text{CH}_3\text{NH}_3\text{PbI}_3$ and $\text{CH}_3\text{NH}_3\text{PbI}_{3-x}\text{Cl}_x$. 6(1):31–37. ISSN 1948-7185. URL <http://pubs.acs.org/doi/abs/10.1021/jz502109e>. (Cited on page 21.)
- [46] W. Tress, N. Marinova, T. Moehl, S. M. Zakeeruddin, Mohammad Khaja Nazeeruddin, and M. Grätzel. Understanding the rate-dependent J–V hysteresis, slow time component, and aging in $\text{CH}_3\text{NH}_3\text{PbI}_3$ perovskite solar cells: The role of a compensated electric field. 8(3):995–1004. ISSN 1754-5692, 1754-5706. URL <http://xlink.rsc.org/?DOI=C4EE03664F>. (Cited on pages 21, 59, 62 and 63.)
- [47] Christopher Eames, Jarvist M. Frost, Piers R. F. Barnes, Brian C. O'Regan, Aron Walsh, and M. Saiful Islam. Ionic transport in hybrid lead iodide perovskite solar cells. 6:7497. ISSN 2041-1723. URL <http://www.nature.com/doifinder/10.1038/ncomms8497>. (Cited on page 63.)
- [48] Jun Haruyama, Keitaro Sodeyama, Liyuan Han, and Yoshitaka Tateyama. First-Principles Study of Ion Diffusion in Perovskite Solar Cell Sensitizers. 137(32):10048–10051. ISSN 0002-7863, 1520-5126. URL <http://pubs.acs.org/doi/abs/10.1021/jacs.5b03615>. (Cited on pages 21 and 63.)
- [49] Wan-Jian Yin, Tingting Shi, and Yanfa Yan. Unique Properties of Halide Perovskites as Possible Origins of the Superior Solar Cell Performance. 26(27):4653–4658, . ISSN 09359648. URL <http://doi.wiley.com/10.1002/adma.201306281>. (Cited on pages 21 and 72.)
- [50] Eric T. Hoke, Daniel J. Slotcavage, Emma R. Dohner, Andrea R. Bowring, Hemamala I. Karunadasa, and Michael D. McGehee. Reversible photo-induced trap formation in mixed-halide hybrid perovskites for photovoltaics. 6(1):613–617. ISSN 2041-6520, 2041-6539. URL <http://xlink.rsc.org/?DOI=C4SC03141E>. (Cited on page 21.)
- [51] Christian Wehrenfennig, Giles E. Eperon, Michael B. Johnston, Henry J. Snaith, and Laura M. Herz. High Charge Carrier Mobilities and Lifetimes in Organolead Trihalide Perovskites. 26

- (10):1584–1589. ISSN 09359648. URL <http://doi.wiley.com/10.1002/adma.201305172>. (Cited on pages 21 and 68.)
- [52] Felix Deschler, Michael Price, Sandeep Pathak, Lina E. Klintberg, David-Dominik Jarausch, Ruben Higler, Sven Hüttner, Tomas Leijtens, Samuel D. Stranks, Henry J. Snaith, Mete Atatüre, Richard T. Phillips, and Richard H. Friend. High Photoluminescence Efficiency and Optically Pumped Lasing in Solution-Processed Mixed Halide Perovskite Semiconductors. 5(8):1421–1426. ISSN 1948-7185. URL <http://pubs.acs.org/doi/abs/10.1021/jz5005285>. (Cited on pages 21 and 75.)
- [53] Platform for all-in-one characterization (PAIOS) by Fluxim AG, Switzerland. URL <http://www.fluxim.com>. (Cited on pages 27, 28 and 29.)
- [54] Semiconducting thin film optics simulator (SETFOS) by Fluxim AG, Switzerland. URL <http://www.fluxim.com>. (Cited on pages 28, 29 and 31.)
- [55] Thomas Lanz, Beat Ruhstaller, Corsin Battaglia, and Christophe Ballif. Extended light scattering model incorporating coherence for thin-film silicon solar cells. 110(3):033111. URL <http://scitation.aip.org/content/aip/journal/jap/110/3/10.1063/1.3622328>. (Cited on page 31.)
- [56] R. Häusermann, E. Knapp, M. Moos, N. A. Reinke, T. Flatz, and B. Ruhstaller. Coupled optoelectronic simulation of organic bulk-heterojunction solar cells: Parameter extraction and sensitivity analysis. 106(10):104507. ISSN 00218979. URL <http://scitation.aip.org/content/aip/journal/jap/106/10/10.1063/1.3259367>. (Cited on page 31.)
- [57] Philipp Löper, Michael Stuckelberger, Bjoern Niesen, Jérémie Werner, Miha Filipič, Soo-Jin Moon, Jun-Ho Yum, Marko Topič, Stefaan De Wolf, and Christophe Ballif. Complex Refractive Index Spectra of $\text{CH}_3\text{NH}_3\text{PbI}_3$ Perovskite Thin Films Determined by Spectroscopic Ellipsometry and Spectrophotometry. 6(1):66–71. ISSN 1948-7185. URL <http://pubs.acs.org/doi/abs/10.1021/jz502471h>. (Cited on page 31.)
- [58] Martin T. Neukom, Nils A. Reinke, Kai A. Brossi, and Beat Ruhstaller. Transient photocurrent response of organic bulk heterojunction solar cells. In *SPIE Photonics Europe*, pages 77220V–77220V. International Society for Optics and Photonics, . URL <http://proceedings.spiedigitallibrary.org/proceeding.aspx?articleid=749468>. (Cited on page 33.)
- [59] M.T. Neukom, N.A. Reinke, and B. Ruhstaller. Charge extraction with linearly increasing voltage: A numerical

- model for parameter extraction. 85(6):1250–1256, . ISSN 0038092X. URL <http://linkinghub.elsevier.com/retrieve/pii/S0038092X11000818>. (Cited on pages 68, 69 and 72.)
- [60] M.T. Neukom, S. Züfle, and B. Ruhstaller. Reliable extraction of organic solar cell parameters by combining steady-state and transient techniques. 13(12):2910–2916, . ISSN 15661199. URL <http://linkinghub.elsevier.com/retrieve/pii/S1566119912004223>. (Cited on pages 33 and 74.)
- [61] Peter Würfel and Uli Würfel. *Physics of Solar Cells: From Basic Principles to Advanced Concepts*. Physics textbook. Wiley-VCH, 2nd, updated and expanded ed edition. ISBN 978-3-527-40857-3. (Cited on pages 44, 50 and 52.)
- [62] A. Baumann, J. Lorrmann, D. Rauh, C. Deibel, and V. Dyakonov. A New Approach for Probing the Mobility and Lifetime of Photogenerated Charge Carriers in Organic Solar Cells Under Real Operating Conditions. 24(32):4381–4386, . ISSN 09359648. URL <http://doi.wiley.com/10.1002/adma.201200874>. (Cited on page 49.)
- [63] G. Dennler, A.J. Mozer, G. Juška, A. Pivrikas, R. Österbacka, A. Fuchsbaauer, and N.S. Sariciftci. Charge carrier mobility and lifetime versus composition of conjugated polymer/-fullerene bulk-heterojunction solar cells. 7(4):229–234. ISSN 15661199. URL <http://linkinghub.elsevier.com/retrieve/pii/S1566119906000474>. (Cited on pages 49 and 68.)
- [64] George F. A. Dibb, Mathis-Andreas Muth, Thomas Kirchartz, Sebastian Engmann, Harald Hoppe, Gerhard Gobsch, Mukundan Thelakkat, Nicolas Blouin, Steve Tierney, Miguel Carrasco-Orozco, James R. Durrant, and Jenny Nelson. Influence of doping on charge carrier collection in normal and inverted geometry polymer:fullerene solar cells. 3. ISSN 2045-2322. URL <http://www.nature.com/doi/10.1038/srep03335>. (Cited on page 49.)
- [65] Tomas Leijtens, Samuel D. Stranks, Giles E. Eperon, Rebecka Lindblad, Erik MJ Johansson, Ian J. McPherson, Hakan Rensmo, James M. Ball, Michael M. Lee, and Henry J. Snaith. Electronic properties of meso-superstructured and planar organometal halide perovskite films: Charge trapping, photodoping, and carrier mobility. 8(7):7147–7155. URL <http://pubs.acs.org/doi/abs/10.1021/nn502115k>. (Cited on pages 49, 68 and 71.)
- [66] Thomas Kirchartz and Jenny Nelson. Meaning of reaction orders in polymer:fullerene solar cells. 86(16). ISSN 1098-0121, 1550-235X. URL <http://link.aps.org/doi/10.1103/PhysRevB.86.165201>. (Cited on page 56.)

- [67] A. Baumann, K. Tvingstedt, M. C. Heiber, S. V  th, C. Momblona, H. J. Bolink, and V. Dyakonov. Persistent photovoltage in methylammonium lead iodide perovskite solar cells. 2(8):081501, . ISSN 2166-532X. URL <http://scitation.aip.org/content/aip/journal/aplmater/2/8/10.1063/1.4885255>. (Cited on pages 59 and 60.)
- [68] Samuel D. Stranks, Victor M. Burlakov, Tomas Leijtens, James M. Ball, Alain Goriely, and Henry J. Snaith. Recombination Kinetics in Organic-Inorganic Perovskites: Excitons, Free Charge, and Subgap States. 2(3). ISSN 2331-7019. URL <http://link.aps.org/doi/10.1103/PhysRevApplied.2.034007>. (Cited on pages 59 and 71.)
- [69] Namyoung Ahn, Dae-Yong Son, In-Hyuk Jang, Seong Min Kang, Mansoo Choi, and Nam-Gyu Park. Highly Reproducible Perovskite Solar Cells with Average Efficiency of 18.3% and Best Efficiency of 19.7% Fabricated via Lewis Base Adduct of Lead(II) Iodide. 137(27):8696–8699. ISSN 0002-7863, 1520-5126. URL <http://pubs.acs.org/doi/abs/10.1021/jacs.5b04930>. (Cited on page 59.)
- [70] Jeong-Hyeok Im, In-Hyuk Jang, Norman Pellet, Michael Gr  tzel, and Nam-Gyu Park. Growth of CH₃NH₃PbI₃ cuboids with controlled size for high-efficiency perovskite solar cells. 9(11):927–932, . ISSN 1748-3387, 1748-3395. URL <http://www.nature.com/doi/10.1038/nnano.2014.181>. (Cited on page 59.)
- [71] Brian C. O'Regan, Piers R. F. Barnes, Xiaoe Li, Chunhung Law, Emilio Palomares, and Jose M. Marin-Beloqui. Optoelectronic Studies of Methylammonium Lead Iodide Perovskite Solar Cells with Mesoporous TiO₂ : Separation of Electronic and Chemical Charge Storage, Understanding Two Recombination Lifetimes, and the Evolution of Band Offsets during *J* – *V* Hysteresis. 137(15):5087–5099. ISSN 0002-7863, 1520-5126. URL <http://pubs.acs.org/doi/abs/10.1021/jacs.5b00761>. (Cited on pages 61 and 75.)
- [72] Xingshu Sun, Reza Asadpour, Wanyi Nie, Aditya D. Mohite, and Muhammad A. Alam. A Physics-based Analytical Model for Perovskite Solar Cells. . URL <http://arxiv.org/abs/1505.05132>. (Cited on page 64.)
- [73] Uli Wurfel, Andres Cuevas, and Peter Wurfel. Charge Carrier Separation in Solar Cells. 5(1):461–469. ISSN 2156-3381, 2156-3403. URL <http://ieeexplore.ieee.org/lpdocs/epic03/wrapper.htm?arnumber=6960066>. (Cited on page 66.)
- [74] Jens Reinhardt, Maria Grein, Christian B  hler, Martin Schubert, and Uli W  rfel. Identifying the Impact of Surface Recombina-

- tion at Electrodes in Organic Solar Cells by Means of Electroluminescence and Modeling. 4(11):n/a–n/a. ISSN 16146832. URL <http://doi.wiley.com/10.1002/aenm.201400081>. (Cited on page 66.)
- [75] G. Juška, K. Arlauskas, M. Viliūnas, and J. Kočka. Extraction current transients: New method of study of charge transport in microcrystalline silicon. 84(21):4946, . URL <http://journals.aps.org/prl/abstract/10.1103/PhysRevLett.84.4946>. (Cited on page 68.)
- [76] Sebastian Bange, Marcel Schubert, and Dieter Neher. Charge mobility determination by current extraction under linear increasing voltages: Case of nonequilibrium charges and field-dependent mobilities. 81(3). ISSN 1098-0121, 1550-235X. URL <http://link.aps.org/doi/10.1103/PhysRevB.81.035209>.
- [77] Jens Lorrmann, Bekele Homa Badada, Olle Inganäs, Vladimir Dyakonov, and Carsten Deibel. Charge carrier extraction by linearly increasing voltage: Analytic framework and ambipolar transients. 108(11):113705. URL <http://scitation.aip.org/content/aip/journal/jap/108/11/10.1063/1.3516392>.
- [78] G. Juška, N. Nekrašas, V. Valentinavičius, P. Meredith, and A. Pivrikas. Extraction of photogenerated charge carriers by linearly increasing voltage in the case of Langevin recombination. 84(15), . ISSN 1098-0121, 1550-235X. URL <http://link.aps.org/doi/10.1103/PhysRevB.84.155202>.
- [79] Oskar J. Sandberg, Mathias Nyman, and Ronald Österbacka. Direct determination of doping concentration and built-in voltage from extraction current transients. 15(11):3413–3420. ISSN 15661199. URL <http://linkinghub.elsevier.com/retrieve/pii/S1566119914004194>. (Cited on page 68.)
- [80] Robert Hanfland, Martin A. Fischer, Wolfgang Brütting, Uli Würfel, and Roderick C. I. MacKenzie. The physical meaning of charge extraction by linearly increasing voltage transients from organic solar cells. 103(6):063904. ISSN 00036951. URL <http://scitation.aip.org/content/aip/journal/apl/103/6/10.1063/1.4818267>. (Cited on page 68.)
- [81] Q. Dong, Y. Fang, Y. Shao, P. Mulligan, J. Qiu, L. Cao, and J. Huang. Electron-hole diffusion lengths > 175 nm in solution-grown $\text{CH}_3\text{NH}_3\text{PbI}_3$ single crystals. 347(6225):967–970. ISSN 0036-8075, 1095-9203. URL <http://www.sciencemag.org/cgi/doi/10.1126/science.aaa5760>. (Cited on page 68.)
- [82] Giacomo Giorgi, Jun-Ichi Fujisawa, Hiroshi Segawa, and Koichi Yamashita. Small Photocarrier Effective Masses Featuring Am-

- bipolar Transport in Methylammonium Lead Iodide Perovskite: A Density Functional Analysis. 4(24):4213–4216. ISSN 1948-7185. URL <http://pubs.acs.org/doi/abs/10.1021/jz4023865>. (Cited on page 68.)
- [83] Carlito S. Ponseca, Tom J. Savenije, Mohamed Abdellah, Kaibo Zheng, Arkady Yartsev, Tobjörn Pascher, Tobias Harlang, Pavel Chabera, Tonu Pullerits, Andrey Stepanov, Jean-Pierre Wolf, and Villy Sundström. Organometal Halide Perovskite Solar Cell Materials Rationalized: Ultrafast Charge Generation, High and Microsecond-Long Balanced Mobilities, and Slow Recombination. 136(14):5189–5192. ISSN 0002-7863, 1520-5126. URL <http://pubs.acs.org/doi/abs/10.1021/ja412583t>. (Cited on page 68.)
- [84] Arianna Marchioro, Joël Teuscher, Dennis Friedrich, Marinus Kunst, Roel van de Krol, Thomas Moehl, Michael Grätzel, and Jacques-E. Moser. Unravelling the mechanism of photoinduced charge transfer processes in lead iodide perovskite solar cells. 8(3):250–255. ISSN 1749-4885, 1749-4893. URL <http://www.nature.com/doi/abs/10.1038/nphoton.2013.374>. (Cited on page 68.)
- [85] E. Hendry, M. Koeberg, B. O'Regan, and M. Bonn. Local Field Effects on Electron Transport in Nanostructured TiO₂ Revealed by Terahertz Spectroscopy. 6(4):755–759. ISSN 1530-6984, 1530-6992. URL <http://pubs.acs.org/doi/abs/10.1021/nl0600225>. (Cited on page 68.)
- [86] Siegfried W. Kettlitz, Jan Mescher, Nico S. Christ, Mirco Nintz, Sebastian Valouch, Alexander Colmann, and Uli Lemmer. Eliminating RC-Effects in Transient Photocurrent Measurements on Organic Photodiodes. 25(7):682–685. ISSN 1041-1135, 1941-0174. URL <http://ieeexplore.ieee.org/lpdocs/epic03/wrapper.htm?arnumber=6461386>. (Cited on pages 69 and 72.)
- [87] Andreas Baumann, Stefan Väh, Philipp Rieder, Michael C. Heiber, Kristofer Tvingstedt, and Vladimir Dyakonov. Identification of Trap States in Perovskite Solar Cells. 6(12):2350–2354. ISSN 1948-7185. URL <http://pubs.acs.org/doi/abs/10.1021/acs.jpcllett.5b00953>. (Cited on page 71.)
- [88] Evelyn Knapp and Beat Ruhstaller. The role of shallow traps in dynamic characterization of organic semiconductor devices. 112(2):024519. ISSN 00218979. URL <http://scitation.aip.org/content/aip/journal/jap/112/2/10.1063/1.4739303>. (Cited on page 72.)
- [89] Jarvist M. Frost, Keith T. Butler, Federico Brivio, Christopher H. Hendon, Mark van Schilfgaarde, and Aron Walsh. Atomistic

- Origins of High-Performance in Hybrid Halide Perovskite Solar Cells. 14(5):2584–2590, . ISSN 1530-6984, 1530-6992. URL <http://pubs.acs.org/doi/abs/10.1021/nl500390f>. (Cited on page 75.)
- [90] M. Hirasawa, T. Ishihara, T. Goto, K. Uchida, and N. Miura. Magnetoabsorption of the lowest exciton in perovskite-type compound (CH₃NH₃)PbI₃. 201:427–430. ISSN 09214526. URL <http://linkinghub.elsevier.com/retrieve/pii/0921452694911304>. (Cited on page 75.)
- [91] Shuangyong Sun, Teddy Salim, Nripan Mathews, Martial Duchamp, Chris Boothroyd, Guichuan Xing, Tze Chien Sum, and Yeng Ming Lam. The origin of high efficiency in low-temperature solution-processable bilayer organometal halide hybrid solar cells. 7(1):399–407, . ISSN 1754-5692, 1754-5706. URL <http://xlink.rsc.org/?DOI=C3EE43161D>. (Cited on page 75.)
- [92] Atsuhiko Miyata, Anatolie Mitiglu, Paulina Plochocka, Oliver Portugall, Jacob Tse-Wei Wang, Samuel D. Stranks, Henry J. Snaith, and Robin J. Nicholas. Direct Measurement of the Exciton Binding Energy and Effective Masses for Charge carriers in an Organic-Inorganic Tri-halide Perovskite. URL <http://arxiv.org/abs/1504.07025>. (Cited on page 75.)
- [93] Tracy Benillouz. Perovskite Stability Demonstrated. URL https://www.dyesol.com/media/wysiwyg/Documents/2015-asx-announcements/2015-05-11-DYE0379_-_Stability_1000_Hours.pdf. (Cited on page 81.)
- [94] Miha Filipič, Philipp Löper, Bjoern Niesen, Stefaan De Wolf, Janez Krč, Christophe Ballif, and Marko Topič. CH₃NH₃PbI₃ perovskite / silicon tandem solar cells: Characterization based optical simulations. 23(7):A263. ISSN 1094-4087. URL <https://www.osapublishing.org/oe/abstract.cfm?uri=oe-23-7-A263>. (Cited on page 81.)
- [95] Colin D. Bailie, M. Greyson Christoforo, Jonathan P. Mailoa, Andrea R. Bowring, Eva L. Unger, William H. Nguyen, Julian Burschka, Norman Pellet, Jungwoo Z. Lee, Michael Grätzel, Rommel Noufi, Tonio Buonassisi, Alberto Salleo, and Michael D. McGehee. Semi-transparent perovskite solar cells for tandems with silicon and CIGS. 8(3):956–963. ISSN 1754-5692, 1754-5706. URL <http://xlink.rsc.org/?DOI=C4EE03322A>. (Cited on page 81.)
- [96] Lukas Kranz, Antonio Abate, Thomas Feurer, Fan Fu, Enrico Avancini, Johannes Löckinger, Patrick Reinhard, Shaik M. Za-keeruddin, Michael Grätzel, Stephan Buecheler, and Ayodhya N. Tiwari. High-Efficiency Polycrystalline Thin Film Tandem Solar Cells. 6(14):2676–2681. ISSN 1948-7185. URL <http://>

pubs.acs.org/doi/abs/10.1021/acs.jpclett.5b01108. (Cited on page 81.)

- [97] Steve Albrecht, Michael Saliba, Juan Pablo Correa Baena, Felix Lang, Lukas Kegelmann, Mathias Mews, Ludmilla Steier, Antonio Abate, Jörg Rappich, Lars Korte, Rutger Schlatmann, Mohammad Khaja Nazeeruddin, Anders Hagfeldt, Michael Grätzel, and Bernd Rech. Monolithic perovskite/silicon-heterojunction tandem solar cells processed at low temperature. ISSN 1754-5692, 1754-5706. URL <http://xlink.rsc.org/?DOI=C5EE02965A>. (Cited on page 81.)

